STRUCTURAL HEALTH MONITORING OF FILAMENT WOUND GLASS FIBER/EPOXY COMPOSITES WITH CARBON BLACK FILLER VIA ELECTRICAL IMPEDANCE TOMOGRAPHY

by

Akshay Jacob Thomas

A Thesis

Submitted to the Faculty of Purdue University

In Partial Fulfillment of the Requirements for the degree of

Master of Science in Aeronautics and Astronautics

School of Aeronautics & Astronautics

West Lafayette, Indiana

August 2019

THE PURDUE UNIVERSITY GRADUATE SCHOOL
STATEMENT OF COMMITTEE APPROVAL

Dr. Tyler Tallman, Chair

Department of Aeronautics and Astronautics

Dr. Vikas Tomar

Department of Aeronautics and Astronautics

Dr. Wenbin Yu

Department of Aeronautics and Astronautics

Approved by:

Dr. Weinong Chen

Head of the Graduate Program

For Shilpa

ACKNOWLEDGMENTS

First and foremost, I would like to thank to thank my advisor, Dr. Tyler Tallman. I express my sincere gratitude to Dr. Tallman for giving me the opportunity to work in his lab on the exciting topic on conductivity based health monitoring. I feel truly lucky to have had such an outstanding advisor. Thank you, Dr. Tallman.

This research was a collaborative effort with Dr. Charles Bakis and his graduate student, Jeff Kim, at Pennsylvania State University. I gratefully thank Dr. Bakis and Jeff for manufacturing the specimen used in this research.

I express my sincere gratitude to my lab mates, Hashim Hassan, Goon Mo Koo and Julio Hernandez. I thank them for the fruitful discussions we had about research but more importantly for being amazing friends and helping me get through grad school.

I also express my sincere gratitude to Dr. R. Byron Pipes and Dr. Michael Bogdanor for giving me the opportunity to explore the world of composites even more. My time at the Composites Manufacturing and Simulation Center was extremely exciting and challenging. Thank you Dr. Pipes and Dr. Bogdanor.

Finally, I would like to thank my parents. For being excellent role models and helping me get up when I was down, thank you.

TABLE OF CONTENTS

LIST OF FIGURES

LIST OF ABBREVIATIONS

BVID	barely visible impact damage
CB	carbon black
CFRP	carbon fiber reinforced polymer
CNF	carbon nanofiber
CNT	carbon nanotube
DAQ	data acquisition
ECC	engineered cementitious composites
EIT	electrical impedance tomography
FBG	fiber bragg grating
GFRP	glass fiber reinforced polymer
MWCNT	multi wall carbon nanotube
NDE	non-destructive evaluation
PANI	polyaniline
PSS	polysodium styrene-4-sulfonate
PU	polyurethane
PVA	polyvinyl alcohol
PVC	polyvinyl chloride
PVDF	polyvinylidene fluoride
SHM	structural health monitoring
VARTM	vacuum assisted resin transfer molding

ABSTRACT

Author: Jacob Thomas, Akshay. MSAAE
Institution: Purdue University
Degree Received: August 2019
Title: Structural Health Monitoring of Filament Wound Glass Fiber/Epoxy Composites with Carbon Black Filler via Electrical Impedance Tomography.
Committee Chair: Tyler Tallman

Fiber reinforced polymer composites are widely used in manufacturing advanced light weight structures for the aerospace, automotive, and energy sectors owing to their superior stiffness and strength. With the increasing use of composites, there is an increasing need to monitor the health of these structures during their lifetime. Currently, health monitoring in filament wound composites is facilitated by embedding piezoelectrics and optical fibers in the composite during the manufacturing process. However, the incorporation of these sensing elements introduces sites of stress concentration which could lead to progressive damage accumulation. In addition to introducing weak spots in the structure, they also make the manufacturing procedure difficult.

Alternatively, nanofiller modification of the matrix imparts conductivity which can be leveraged for real time health monitoring with fewer changes to the manufacturing method. Well dispersed nanofillers act as an integrated sensing network. Damage or strain severs the well-connected nanofiller network thereby causing a local change in conductivity. The self-sensing capabilities of these modified composites can be combined with low cost, minimally invasive imaging modalities such as electrical impedance tomography (EIT) for damage detection. To date, however, EIT has exclusively been used for damage detection in planar coupons. These simple plate-like structures are not representative of real-world complex geometries. This thesis advances the state of the art in conductivity-based structural health monitoring (SHM) and nondestructive evaluation (NDE) by addressing this limitation of EIT. The current study will look into damage detection of a non-planar multiply connected domain – a filament-wound glass fiber/epoxy tube modified by carbon black (CB) filler. The results show that EIT is able to detect through holes as small as 7.94 mm in a tube with length-to-diameter ratio of 132.4 mm-to-66.2 mm (aspect ratio of 2:1). Further, the sensitivity of EIT to damage improved with decreasing tube aspect ratio. EIT was also successful in detecting sub-surface damage induced by low velocity impacts. These results indicate that EIT

has much greater potential for composite SHM and NDE than prevailing work limited to planar geometries suggest.

1. LITERATURE REVIEW

1.1 Introduction

Laminated composites are widely used as high performance structural materials owing to their superior strength, low weight, and excellent fatigue properties. As an example, composite tubes are used for building stronger and lighter pressure vessels [1] and corrosion resistant piping systems [2]. Despite their numerous advantages, composites are susceptible to complex damage not seen in traditional alloys. Phenomena such as delamination are specific to composite materials and can be of catastrophic consequence, especially in the aerospace sector where safety is of paramount importance. However, detection of such types of damage is difficult since they generally manifest below the surface. Since such sub-surface damage is outwardly invisible, addressing these issues are very important in composites research.

To that end, extensive research has been done on understanding the response of composite tubes under various loading conditions. For instance, Bakaiyan et al. studied the structural response of filament wound composites subject to internal pressure and thermo-mechanical loading [3]. Gemi et al. studied the effect of stacking sequence on low velocity impact response and damage formation in hybrid composite pipes under internal pressure [4]. Extensive research has been conducted on mechanical response and damage in literature. Since low velocity impacts are an important consideration for composite structures (leading to barely visible damage), the studies in [5]–[10] show extensive research for damage levels and residual strengths of composite tubes.

Predicting all loading conditions and having exhaustive knowledge on damage initiation and propagation is an insurmountable task. As an alternative, SHM is gaining traction. SHM is the method of continuously monitoring the health of the structure during its lifetime and providing valuable insights into its integrity and probability of failure. SHM for fiber reinforced polymer composites need to have sensitivity to matrix cracks, delamination, and fiber breakage. These methods should be able to detect the onset of damage to ensure safe operation of the structure.

Consider first, composite SHM via vibration testing. Vibration testing generally involves exciting the structure at frequencies that engage low-order modes or natural frequencies. Damage is expected to cause a local reduction in stiffness that causes a change in mode shapes or natural frequency. These methods, however, are insensitive to initial signs of damage and will be unable to detect signs of matrix cracking which could lead to progressive damage accumulation [11], [12].

Another important method of health monitoring in composites tubes are embedding sensors into the cylindrical composite during manufacturing. For instance, optical fibers have been used in strain pattern detection by Choi et al [13]. Fiber Bragg Grating (FBG) sensors have also shown advantages such as having small dimensions, light weight, corrosion resistance [14], [15], and compatibility with manufacturing procedures[16]. On the other hand, Beard et al. used built-in piezoelectric transducers to find structural defects in filament wound composite tubes [17]. However, embedding these sensors introduce sites of stress concentration in the composite and failure is most likely to initiate at these points. Furthermore, damage sufficiently removed from the position of these sensors might go undetected.

Guided wave techniques such as Lamb wave tomography studies structures with wavelengths that are small enough to detect matrix cracking [18]. However, guide wave methods require the incorporation of sensors/actuators to be embedded in the structure which can be difficult in fiber reinforced composites.

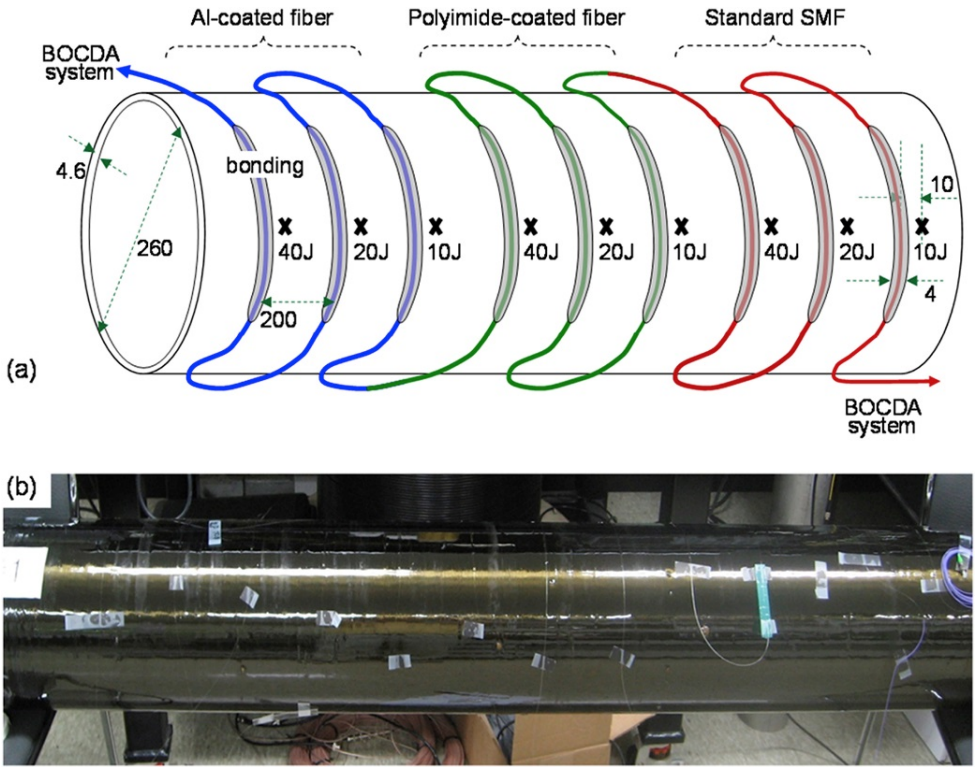

Figure 1.1: Experiemntal setup using optical fibers for impact detection mentioned in [13].

Conductivity-based SHM has also received attention in carbon fiber reinforced polymers (CFRP). The carbon fiber acts as conducting phase and any fiber breakage causes a loss of conductivity [19], [20]. However, these methods are sensitive only to loss in conductivity caused by the fiber breakage and remain insensitive to matrix damage. Thus matrix cracking and delamination could go undetected.

As an alternative to the above mentioned methods, the self-sensing capabilities of nanofiller modified matrix composites have received much attention in the health monitoring community. Nanofillers form well connected percolating networks in the matrix phase of the composite which acts an integrated circuit in the composite. Any damage that severs the well-connected network causes a local change in conductivity which can be directly related to a state of mechanical damage. The nanofillers dispersed throughout the composite ensure sensitivity to damage at any location in the composite. These nanofillers are of negligible weight and hold potential for health monitoring in applications where weight savings are important.

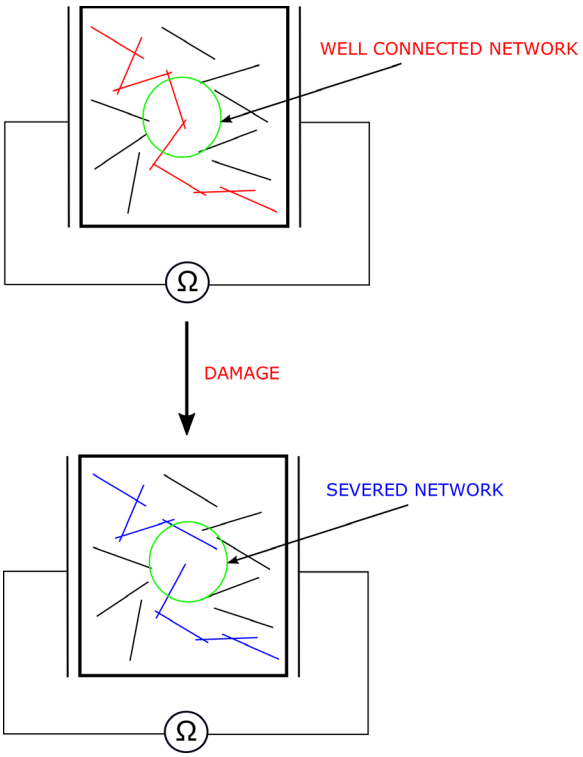

Figure 1.2: Schematic showing damage induced conductivity loss. Top: Nanofillers are well dispersed in a matrix. The well connected network is shown in red. Bottom: Nanofiller network post damage. The blue lines indicate the severed nanofiller network.

The following sections discuss the current state of the art nanofiller-enabled conductivity-based SHM. Before discussing conductivity based SHM, however, an introduction to nanocomposites is presented first.

1.2 Nanocomposites

Nanocomposites, as the term suggests, are multiphase materials encompassing fillers at the nanoscale level. Extensive details regarding nanofillers are not included in this study and readers are directed to [21]. Typically, these nanofillers include carbon nanotubes (CNTs), carbon nanofibers (CNFs), and carbon black (CB).

CNTs have received attention owing to their excellent mechanical properties [22], [23], electrical conductivity [24],and thermal properties [22]. CNTs, structurally, are high aspect ratio, single or

multiple concentric cylinders of graphene [25]. CNTs have shown potential for enhancing mechanical properties [26], [27], and improving damping properties [28]. CNFs are similar to CNTs in terms of high aspect ratios ranging from 250 – 2000 [22]. CNFs are cheaper compared to CNTs and have similar properties of electrical conductivity and provide good levels of mechanical enhancement [26], [29].

Even though the high aspect ratio of CNTs and CNFs allow to attain percolation at low filler concentrations [30], [31], CB is preferred in manufacturing fiber reinforced composites. This is attributed to the fact the high aspect ratio of CNTs and CNFs pose difficulties in dispersing them in the matrix without entanglement. On the other hand, CB fillers from stacks of hexagonal carbon tings with much lower aspect ratios enabling easier dispersion among structural fibers [32].

1.3 Nanocomposite Conductivity

Since this study leverages the conductive property of nanofiller modified composites, it is worthwhile understanding the mechanisms behind electrical conductivity. Nanocomposites depend on well-connected networks of nanofillers for electrical conductivity. Any severance to this well connected network can cause a change in the electrical conductivity of the composite. Electrical conductivity in nanocomposites depends on the existence of electrically percolated nanofiller networks. Electrical percolation means a well distributed network such that electrons can travel from filler-to-filler and throughout the nanocomposite. The fillers are not required to be in direct physical contact to form a well-connected network. They are able to tunnel through a small distance in the insulating matrix phase on to a nanofiller in proximity thereby enabling nanocomposite conductivity. Filler-filler distance is an important factor for electron tunneling and hence enabling piezoresistivity in nanocomposites. The equivalent resistance between neighboring fillers is a function of their separation [33].

An extensive survey on the percolation threshold has been conducted in [34]. The review shows that electrical percolation is not only dependent on the filler weight fraction, but also on the processing methods used. The existence of two percolating thresholds were also reported by Kovacs et al. [35].

Nanocomposites have received considerable attention in terms of modeling their piezoresistivity property. With advanced nanoscale manufacturing methods available, it is vital to understand the conductivity mechanisms in order to implement conductivity based SHM on large scale. Modeling piezoresistive nanocomposites have received attention to their potential use in, for example, sensing skins for structures [36] [34]. An experimental investigations by Hu et.al [36] on piezoresistivity is shown in Figure (1.3).

Figure (1.3) shows the change in resistance of the sensing skin with increasing strain. The effect of different weight fractions on the change in resistance is also shown. Another interesting electrical property of nanocomposites is anisotropic conductivity through nanofiller alignment, generally achieved by either mechanical or electrical tailoring. For example, Thostenson and Chou extruded polymer melts to obtain highly aligned nanocomposite films [37], where they studied the effects of alignment of carbon nanotubes to obtain higher elastic moduli. Gungor and Bakis applied strong electric fields prior to curing of the composite to obtain better electrical percolation in the through thickness direction [38].

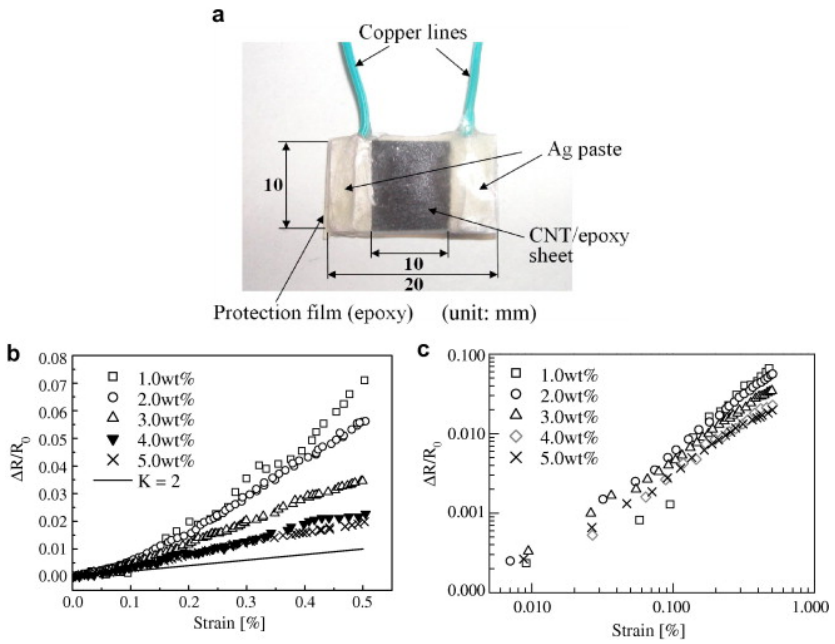

Figure 1.3: From [36]. Experimental piezoresistivity of polymer/CNT nanocomposite strain sensor: (a) polymer/CNT nanocomposite strain sensor; (b) experimental piezoresistivity in the polymer with different CNT loadings; and (c) log plot of experimental piezoresistivity.

1.4 Nanocomposite Resistance Change Methods

Having discussed conductivity mechanisms in nanocomposites, this section discusses the current state of the art in piezoresistive SHM. First, SHM in simple one dimensional specimens will be discussed followed by a discussion on the two-dimensional plate-like structures. Finally, tomographic methods in literature for damage detection in structures will be presented.

1.4.1 Resistance Change Methods in Beam Specimens

As discussed earlier, nanofillers dispersed in the matrix phase of the composite acts as a network for self-sensing. The major advantage of such structures is it circumvents the need for external sensors for health monitoring. The simplest type of structure to be studied is a one dimensional beam structure. In these type of structures, the resistance is measured at two different points along the length of the beam before and after a damage occurrence or any introduction of strain. This method provides valuable insights into the occurrence of damage initiation and correlations can be made between resistance change and damage accumulation and propagation. A considerable increase in resistance can be observed after failure of the specimen and the resistance values do not return back to its original values. The permanent change in resistance values is attributed to cracking of the matrix phase, which is irreversible. Resistance continues to accumulate after failure has initiated. These observation agree with intuition that the fillers are permanently displaced after failure initiation. Despite the fact that measuring resistance between two points only provides information of damage between the measuring points, it is worthwhile looking at the resistance change methods in literature as it builds intuition in conductivity based SHM.

As an example of this approach, Thostenson and Chou [39] manufactured an unidirectional glass fiber/epoxy laminate modified with multi walled carbon nanotubes (MWCNTs). An artifact in the form of a cut was made in the center ply to initiate delamination. The discontinuity at the center ply results in accumulation of shear stresses which initiate delamination. The specimen was loaded and the resistance change was linear until the initiation of delamination, after which a sharp increase in resistance occured. A marked increase of the slope of the resistance change was observed indicating the extension of the ply delamination. A $[0/90]_s$ laminate was subjected to similar loading and a similar change in resistance was observed. It was observed that the change

in resistance was markedly greater than the loss in stiffness of the specimen. This is shown on the graph in Figure (1.4)

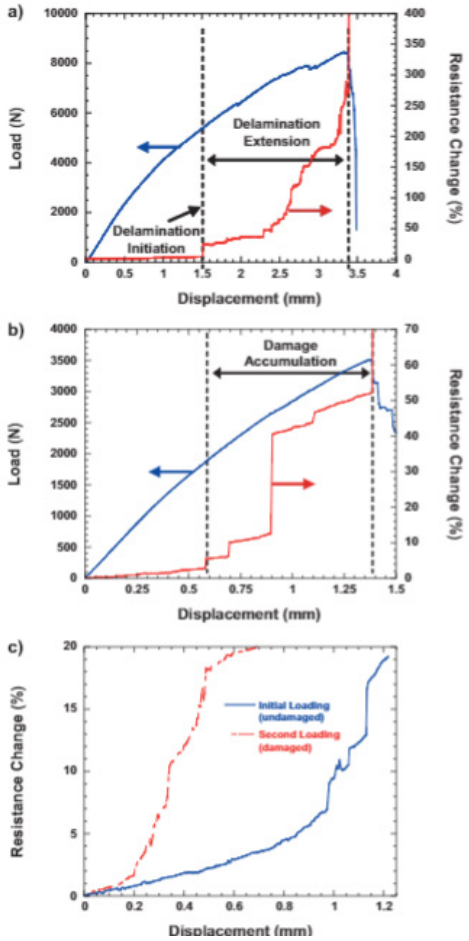

Figure 1.4: (a) Load displacement curves for the unidirectional laminate with center ply cut (b) load displacement curves for 0/90 specimen (c) resistance curves for initial loading (undamaged) and reloading (damaged) laminates. Studies made in [39].

As another example, Gao, Thostenson, Zhang, and Chou [40] manufactured cross-ply E-glass/vinyl ester $[0/90]_s$ laminates with CNTs. The CNTs were first dispersed in the vinyl ester and the mixture was drawn into the preform via vacuum assisted resin transfer molding (VARTM). Quasi-static and cyclic tensile loading tests were conducted during which specimen resistance change and acoustic emission count were recorded. During initial quasi-static loading of the undamaged specimen, the resistance response and the acoustic emission trends were similar. However, on repeating the quasi-static loading, the trends for the acoustic counts and resistance change were different. This is because reloading reopens cracks that produce no acoustic events.

Incremental cyclic loading produced resulted in increased unloaded resistance which mark the formation of permanent damage. Acoustic emission counts also increased with increased cyclic increments implying the formation of cracks evident from resistance changes.

And as a final example, Gao et al. [41] studied the effects of impacts on resistance change in epoxy/plain glass fiber containing CNTs. The composite was cut in sections measuring 10.2 cm × 15.2 cm. Silver paint electrodes were then applied on the 10.2 cm edges, thereby measuring changes along the 15.2 cm length. Impacts of energy 70 J were induced in the center of the plate and the resistance changes were measured for repeated impact loading. It was found that resistance increased with each new impact and a change up to 120% in resistance was observed after 11 loadings.

1.4.2 Resistance Change Methods in Plate Specimens

Resistance change methods in plate specimens are an intuitive extension of the work previously discussed for one-dimensional specimens. The simplest approach to locating damage in a fiber reinforced plate with nanofiller-modified matrices is to line the specimen with an array or grid of electrodes. Resistance between neighboring electrode pairs are compared before and after damage. Damage can be located via resistance change methods only between the electrode pairs. Applying electrodes to one side of the specimen allows for in-plane damage measurements and applying electrodes to both the sides of the specimen allow for through thickness damage measurement. Through thickness measurements are better suited to locating sub-surface damage and damage simulated by drilling holes are located via in-plane measurements. A large number of electrodes are required for high resolution images.

Zhang et al. [42] studied 2 wt% CB-modified glass fiber/epoxy laminates. Laminates were made with 2 wt % CB and 2 wt% CB and copper chloride (CC). Unidirectional specimens were made to measure Mode I and Mode II fracture toughness and electrodes were applied through the width of the specimen to measure through thickness resistance. A departure from linear increase in resistance was observed after the initiation of damage. A $[45/0/-45/90]_s$ laminate was cut to 150 mm × 100 mm and a 9 × 9 grid of electrodes was attached to the top and bottom surface. Attaching

electrodes to the top and bottom enables through thickness measurements. The trimmed plate was subject to drop tower impact tests at 6.7 J/mm. Impact damage was imaged by weighting and interpolating resistance changes. The interpolation serves only for ease of visibility and not as a tomographic method. C-scans verified the damage locations.

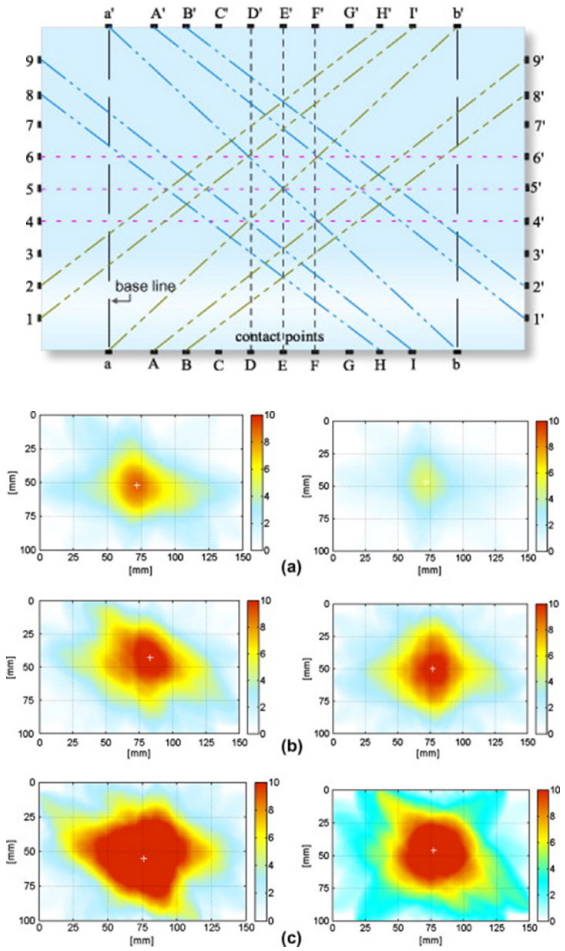

Figure 1.5: In plane measurements by Zhang et al.[42]. Detection of impacts (top to bottom) at 50, 100 and 150 % of 6.7 J/mm for 2 wt% CB (right) and 2 wt% CB and CC (left)

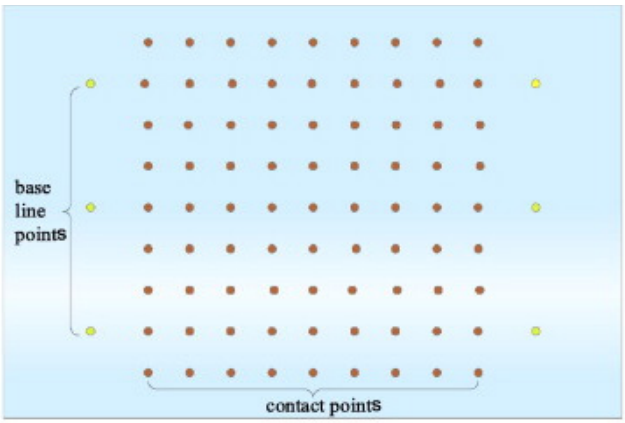

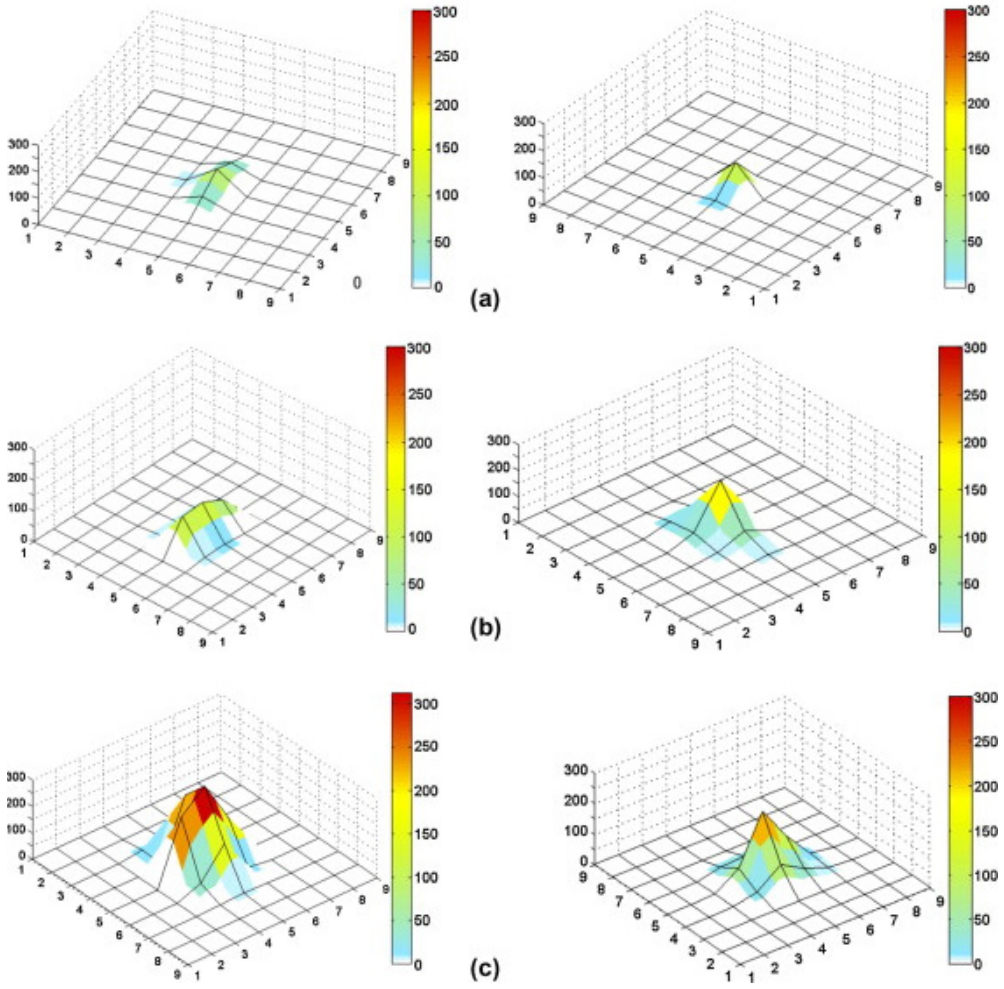

Figure 1.6: Through thickness measurements by Zhang et al. [42] for (top to bottom) at 50, 100, and 150 % of 6.7 J/mm for 2 wt% CB (left) and 2 wt% CB and CC (right)

Viets et al. [43] manufactured a unidirectional, glass fiber/epoxy laminates with 1 wt% MWCNTs and 12 wt% CB. Two plates of dimensions 120 mm × 120 mm × 3 mm were cut out and lines of conductive silver ink were applied on the top and bottom of the laminates. Lines on the top were perpendicular to the fiber direction and lines on the bottom were parallel to the fiber direction. Resistance measurements were taken through the thickness. The plates were impacted with an energy of 7.65 J. A map of resistance change was created by measuring resistance before and after impact and interpolating these resistance changes. Figure (1.7) shows the electrode placement and resulting impact damage detection results.

1.4.3 Tomographic Methods – EIT

Although the discussions from previous sections showed that the resistance change methods were able to successfully detect damage in piezoresistive materials, the methods generally require large electrode arrays which might not be possible from an implementation point of view. To that end, EIT has emerged as a potential tool for spatially detecting damage. EIT is able to resolve damage-induced conductivity changes from only boundary voltage data. EIT has been primarily used for biomedical application such as imaging neural [44], [45] and organ activity[45] [46]. Recently however, EIT has been used as a SHM and NDE tool for piezoresistive structures. The following discussion will outline some of the research conducted to spatially detect damage in piezoresistive materials.

Hou et al. [47] first used EIT to image conductivity distributions in CNT thin films. Homogenous nanostructured thin films were fabricated using polyelectrolyte constituents polyaniline (PANI) emeraldine base, polyvinyl alcohol (PVA), and polysodium styrene-4-sulfonate (PSS) via a layer-by-layer assembly method. These specimens were imaged via EIT to detect regions of different conductivity caused by etching. A 32-electrode EIT system was able to accurately locate the etching and also reproduce their geometry. This reconstruction of conductivity is shown in Figure (1.8).

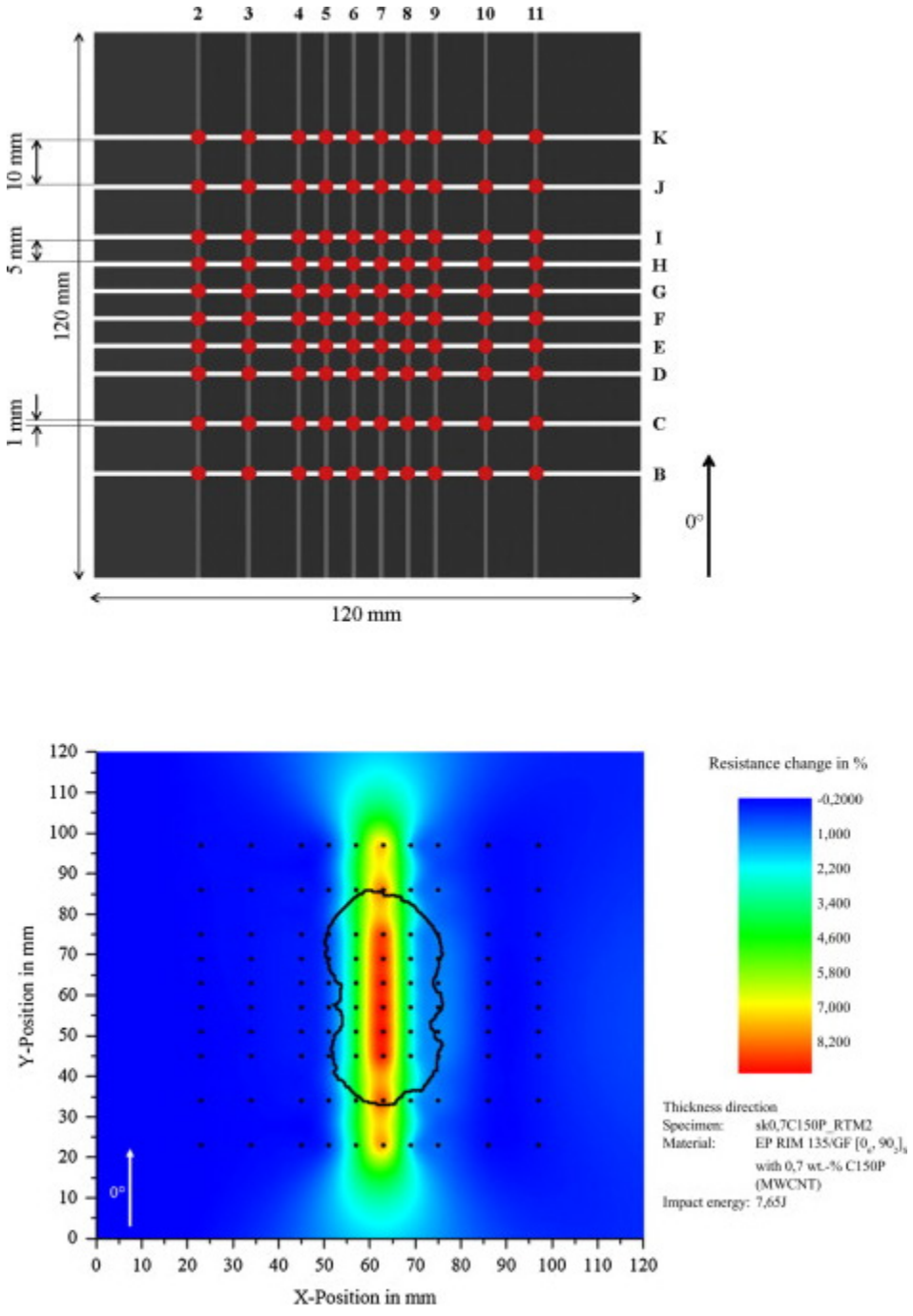

Figure 1.7: Detection of the 7.65 J impact described by Viets et a. in [43]. The black outline shows the delamination detected via the C- scan

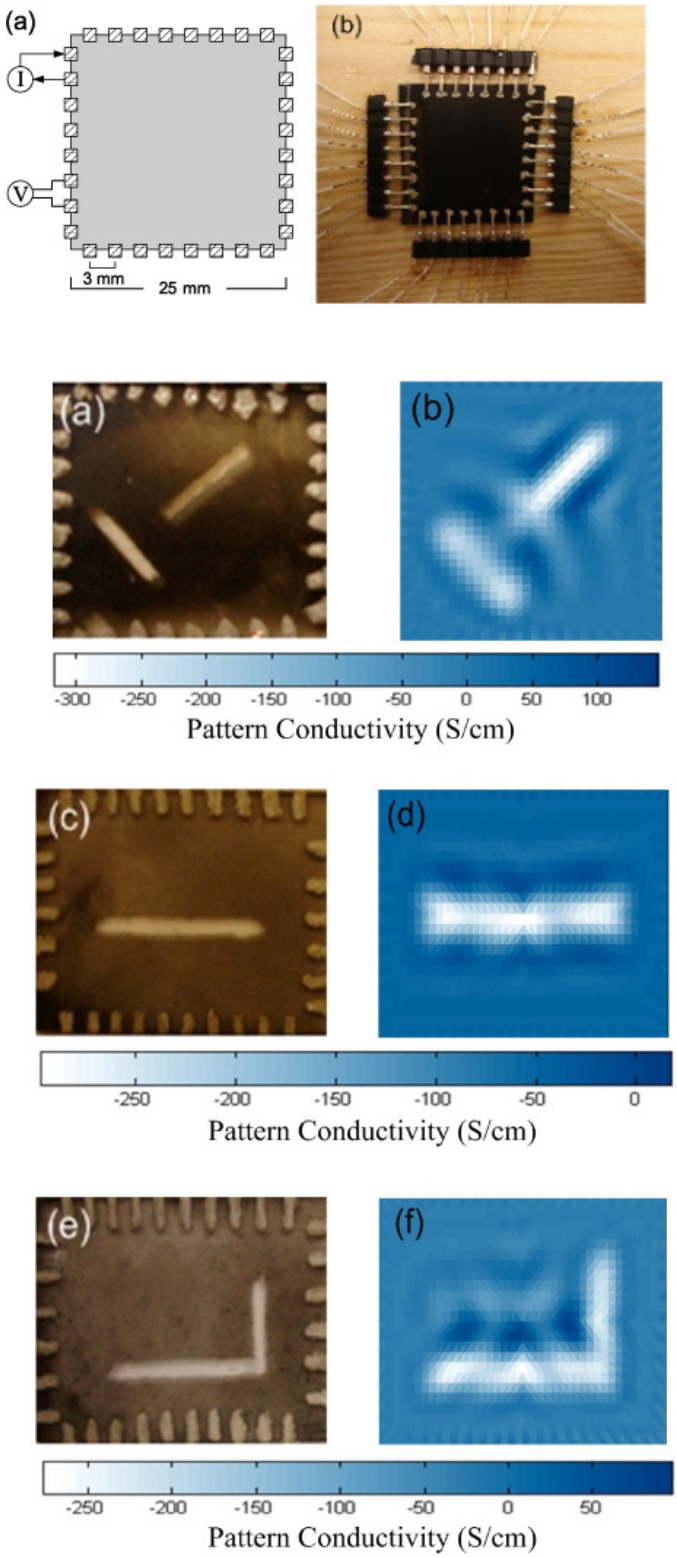

Figure 1.8: Example of EIT reconstructions of etchings in CNT film [47]

EIT has also been used for imaging cracks in cementitious structures in [48] and [49]. Hou et al. in [48] used engineered cementitious composites (ECC) to examine the capability of EIT to detect damage. The specimens were loaded in tension until they cracked. The EIT reconstruction of the crack is shown in Figure (1.9).

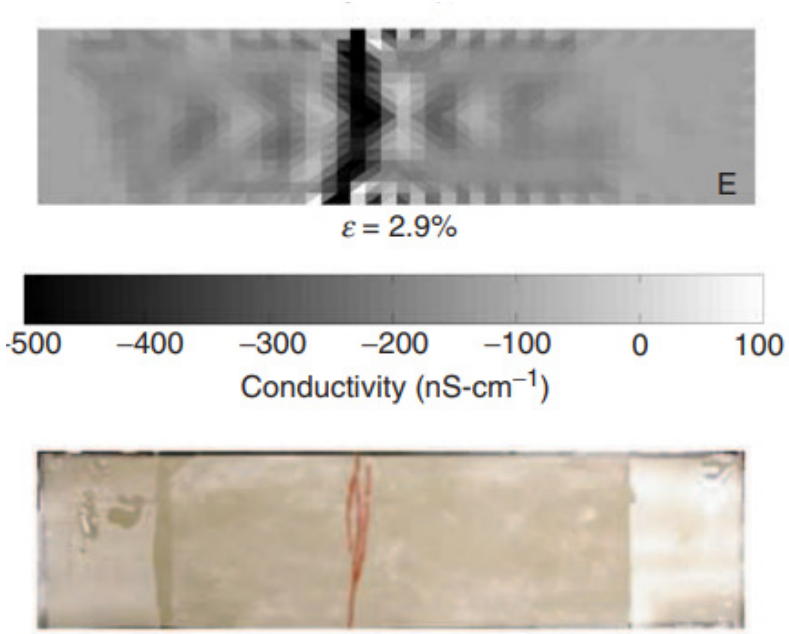

Figure 1.9: Top: EIT reconstruction of an EEC sample cracked under tension [48]. Bottom: The cracked EEC sample

Tallman et al.[50] used EIT for damage detection in fiber reinforced epoxy with CB filler. A 26 layer $[[0/90]_6/0]_s$ laminate was made to attain approximately isotropic conductivity. A sensitivity study was conducted to understand the lower threshold of damage detectability by drilling holes of increasing sizes. Also, multiple holes were drilled at different locations to understand the capability of EIT to detect multiple damage locations. EIT was able to detect through holes as small as 3.18 mm and was also able to detect multiple damage locations. However, EIT lost sensitivity to small damage in the presence of larger damage. Further, to understand the capability of EIT to detect impact damages, a similar specimen was impacted with 50 J via a drop tower. The impact caused an indentation on the specimen and a crack propagating from the impact location. EIT was able to detect not only the impact location but also the crack direction.

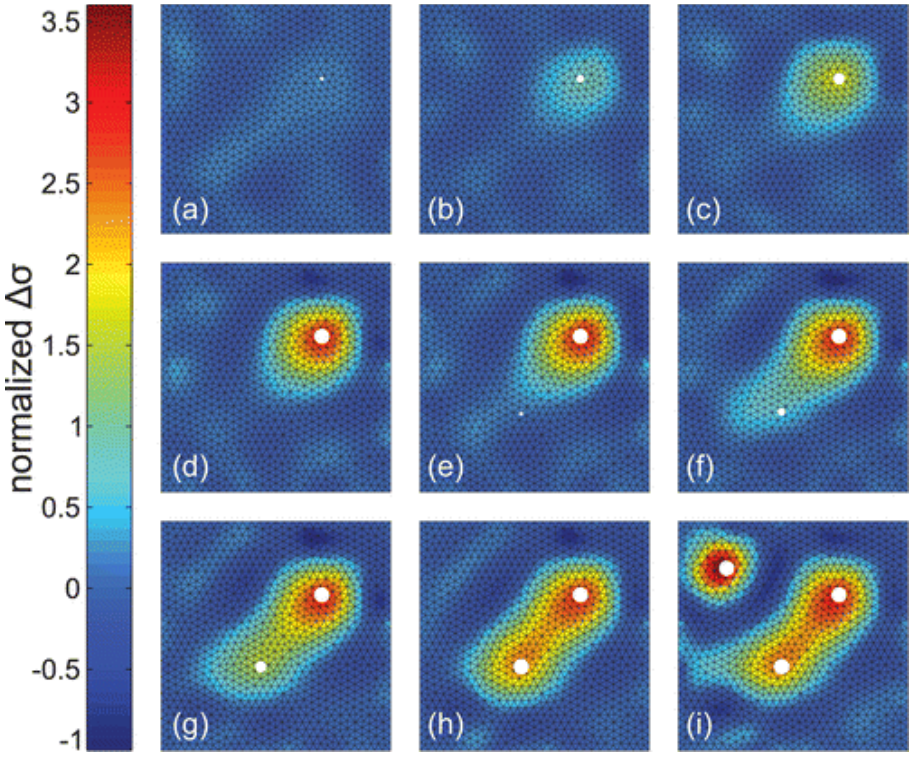

Figure 1.10: Sensitivity and multiple damage detection by Tallman et al [50]. Through hole size and location is indicated by the white circle. Diameters of each through hole are as follows. (a) 1.59 mm (b) 3.18 mm (c) 4.76 mm (d) 6.35 mm (e) 6.35 mm and 1.59 mm (f) 6.35 mm and 3.18 mm (g) 6.35 mm and 4.76 mm (h) 6.35 mm and 6.35 m (i) 6.35, 6.35mm and 6.35 mm

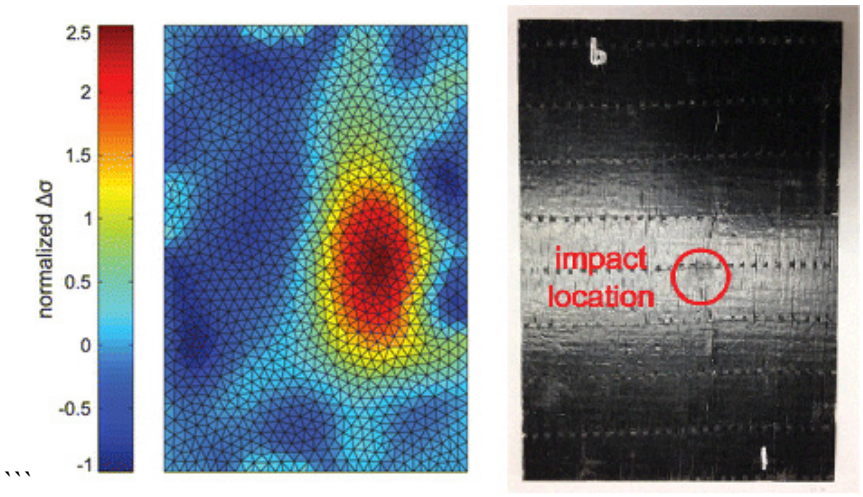

Figure 1.11: Impact damage detection by Tallman et al. [50]. The conductivity artifact running along the length of the plate corresponds with the crack direction.

Tallman et al. also manufactured epoxy plates with 1 wt% CNFs to understand the capability of EIT to detect damage [51]. The filler concentration was chosen to provide maximum conductivity with least increase in mix viscosity. Damage was simulated by drilling a hole of size 6.35 mm. EIT was conducted to find the location of damage. The conductivity reconstructions are shown in Figure (1.12)

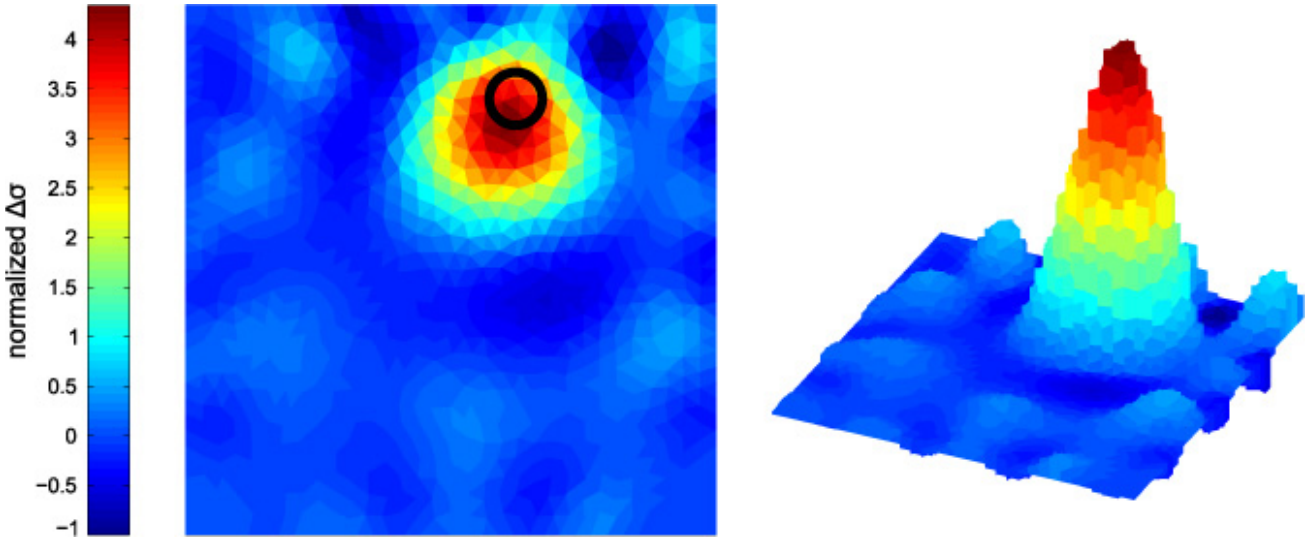

Figure 1.12: Damage detection results by Tallman et al. [51]. The black circle shows the location of the drilled hole.

Loyola et al. [52] manufactured a GFRP composite and sprayed a coating of multi-walled carbon nanotube-polyvinylidene fluoride (MWCNT-PVDF) of varying contrast on to the surface of the GFRP to simulate conductivity changes. The readers are directed to [52] for a detailed understanding of the manufacturing procedure. After the contrasting conductive film was deposited, EIT was used to reconstruct the conductivity distribution. Figure (1.13) shows the GFRP specimen with contrasting MWCNT-PVDF coating and the resulting EIT reconstruction.

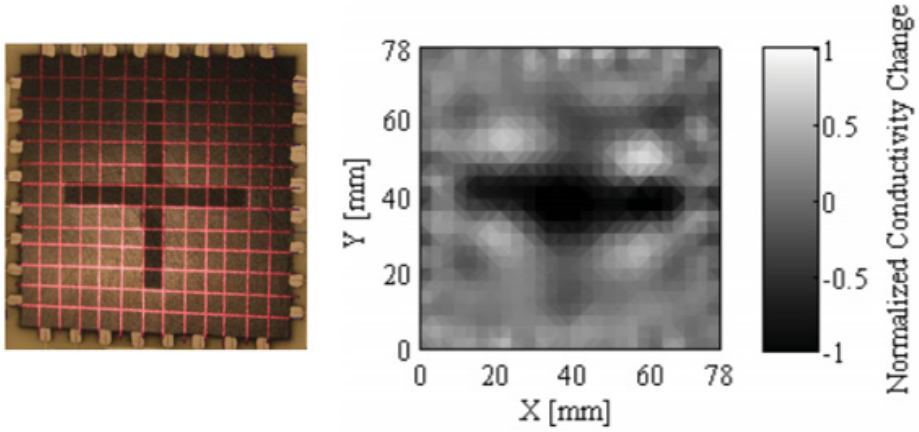

Figure 1.13: Left: GFRP specimen spray coated with MCNT-PVDF film with a masked cross in the center. Right: EIT reconstruction of the contrasting conductivity of the MWCNT-PVDF sprayed specimen [52].

Loyola et al. [53] used a similar approach as used in [52] to detect damage in glass fiber reinforced composite plates. A 16 layer GFRP composite was manufactured via a VARTM process with a layup sequence of $[0/+45/90/-45]_{2s}$. To allow easy access of the sensing layers, the glass fiber mats with the sprayed on MWCNT-PVDF films were only placed on the top and bottom layers with the film facing outwards from the interior of the plate. Damage was simulated by drilling a hole of size 6.35 mm at the center of the plate. The capability of EIT to detect impact induced damage on the plate was also studied. The EIT reconstructions for the through hole is shown in Figure (1.14) and the reconstructions for impact damage are shown in Figure (1.15).

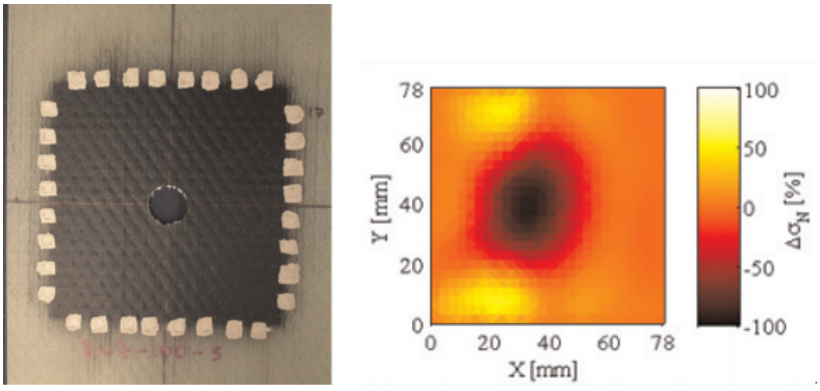

Figure 1.14: Left: GFRP specimen with 6.35 mm hole. Right: EIT reconstruction of the specimen [53]

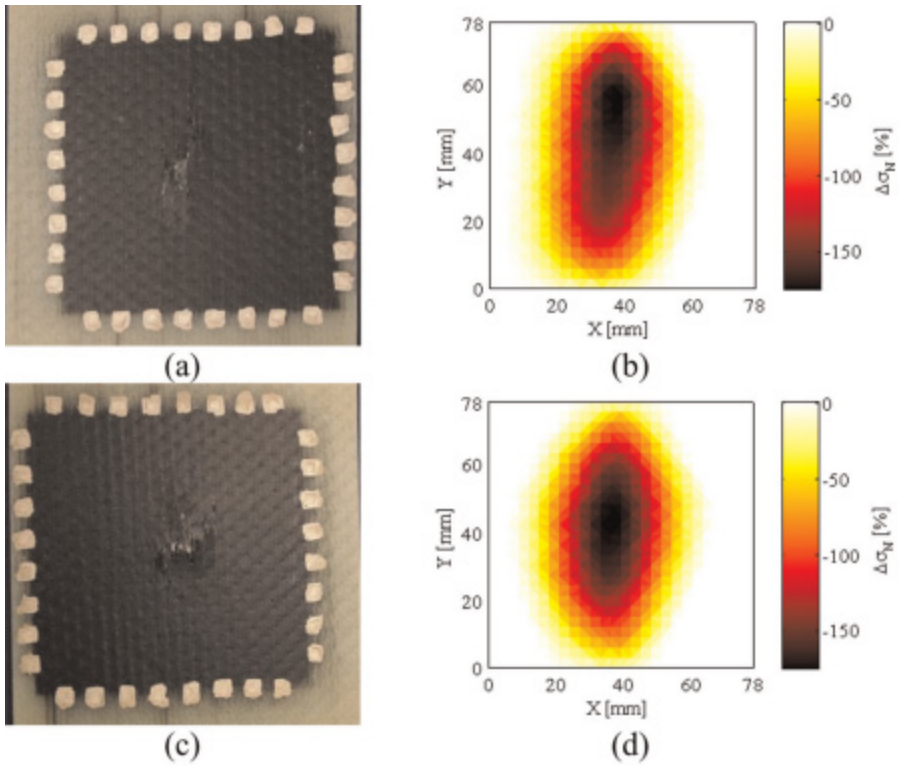

Figure 1.15: (a) Picture and (b) EIT reconstruction of the plate subject to 100 J of impact. (c) Picture and (d) EIT reconstruction of plate subject to 140 J of impact [53].

Hallaji et al. employed EIT to detect the cracking on concrete via a sensing skin approach [54]. The sensing skins were made of copper paint. The paint was applied on to a mortar substrate by spraying as uniformly as possible. A notch was made in the mortar substrate and was subjected to a four point bending test. The specimen is shown in Figure (1.16). EIT reconstructions were made at different times during the testing and the images are shown in Figure (1.17).

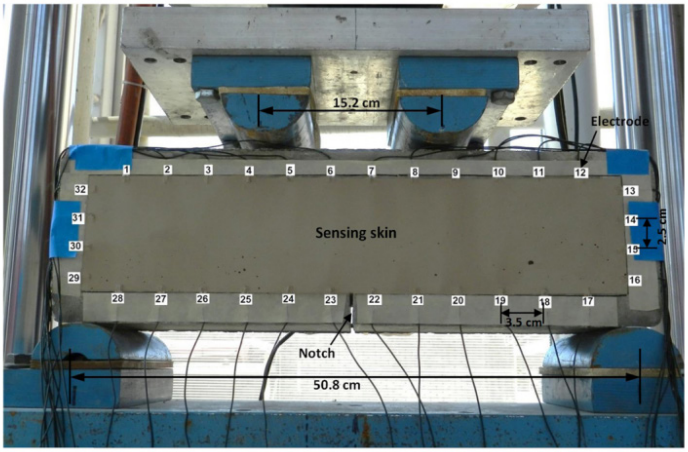

Figure 1.16: Sensing skin applied to mortar specimen with a notch and prepared for four point bending [54].

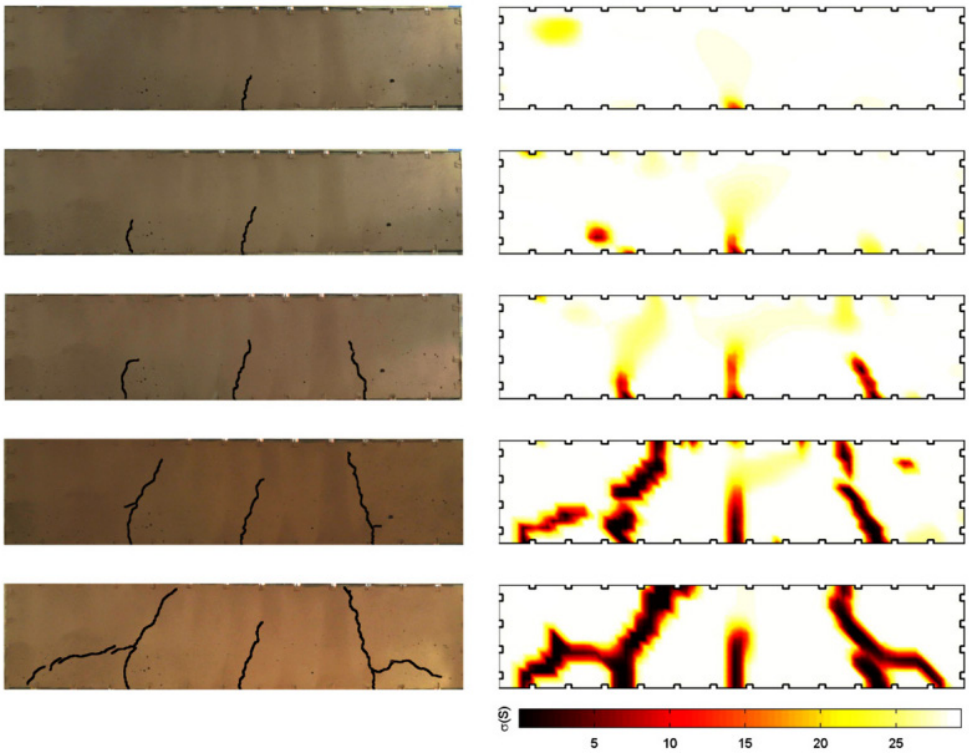

Figure 1.17: EIT reconstructions of sensing skin at five loading states. From top to bottom: row 1: under 18.2 kN load; row 2: under 29.8 kN load; row 3: under 39.1 kN load; row 4: under 71.2 kN load; row 5: under 85 kN load. The images on the left show the sensing skin. The images on the right show the corresponding EIT reconstruction. The black line in the images on the left show the cracks developed during loading [54].

EIT has also been used for damage detection and localization in CFRP composite laminates in [55] and for GF in [56] by an anisotropic conductivity approach. Tallman et al. also used EIT for strain detection in CNF-modified polyurethane [57]. Work has also been conducted to improve EIT for SHM and NDE via nanofiller-induced enhanced sensitivity [58], supplemented sensitivity formulations [59], Gaussian informed regularization [60], and exploring the effect of first and second-order norms of error and regularization [61]. In light of the preceding discussion, we can see that EIT has indeed received considerable attention for SHM and NDE applications. Note, however, that all of these studies were conducted on simple shapes (i.e. thin, plate-like structures).

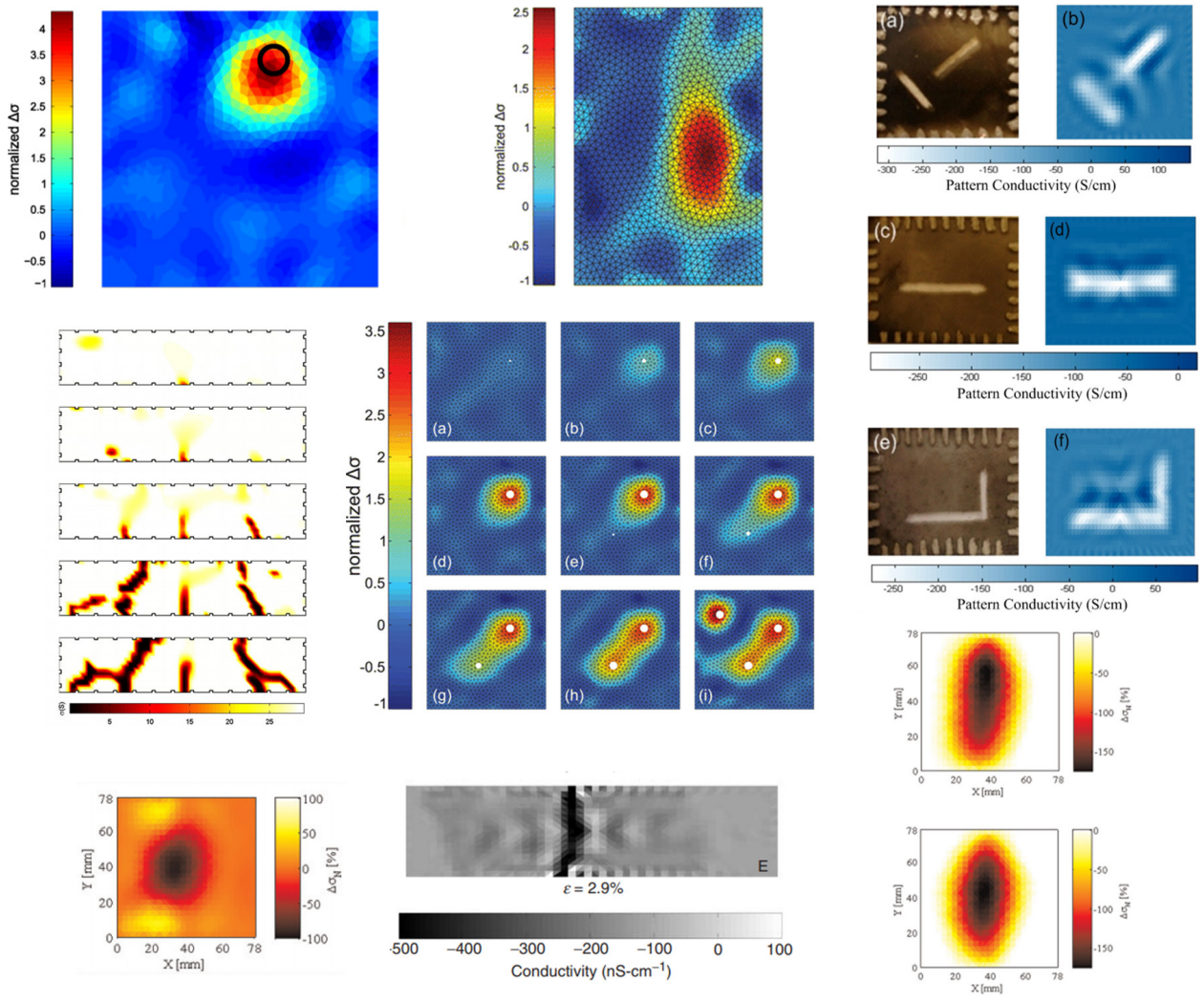

Figure 1.18: EIT reconstructions of specimens taken from [47], [48], [50]–[54]. Note that all these studies have been limited to simple plate-like structures.

2. PROBLEM STATEMENT, RESEARCH GOAL AND THESIS ORGANIZATION

Despite the extensive literature on using EIT for damage detection in structures [47]–[52], [54], [56]–[58], there remains a gap in literature to use EIT for non-planar structures. Chapter 1 showed the application of EIT for damage detection. However the studies were strictly limited to planar structures. Further, there is a compelling need for the SHM of composite tubes. Hence, this thesis work addresses both of these limitations by establishing the potential of EIT for application to complex geometries such as tubes.

Problem Statement

Current methods of SHM using EIT have only looked into damage detection for simple plate-like structures. Simple plate-like structures are not representative of real world geometries. Most structures in the aerospace and automotive sectors are non-planar with complex geometries. Thus, for EIT to be a viable SHM modality, it must be extended to these structurally realistic geometries.

Research Goal

Establish the potential of EIT as a health monitoring modality for self-sensing composite tubes.

Thesis Organization

Having set a goal for the research study, the remainder of the thesis will be organized as follows. First, the manufacturing process of the CB-modified tube will be described. Second, EIT will be introduced and its mathematical formulation presented. Next, experimental damage detection in filament wound glass fiber/epoxy composites using CB filler will be presented. Finally, the results will be encapsulated to understand much broader impacts. And lastly, recommendations for future work will be made.

3. CB-MODIFIED GLASS FIBER/EPOXY MANUFACTURING

A glass fiber/epoxy tube was made by the filament winding technique. S2-Glass fiber rovings with type 449 binder (Advanced Glassfiber Yarns, Aiken, South Carolina) were wetted out with a stoichiometric mixture of diglycidyl ether of bisphenol A diluted with alkyl glycidyl ether (EPON 8132, Miller-Stephenson, Danbury, Connecticut), diethyltoluenediamine (EPIKURE W, Miller-Stephenson, Danbury, Connecticut), and a high-structure CB (Black Pearls 2000, Cabot, Boston, Massachusetts) was added to obtain 1% weight concentration. The epoxy and CB were combined in a beaker and mixed for 15 minutes using a magnetic stirrer rotating at 500 revolutions per minute. The mixture was then sonicated to obtain good dispersion of the carbon black in the epoxy. The mixture was sonicated for 30 minutes using a 900 W, 20 KHz, ultrasonic horn (Branson, Danbury, Connecticut) and further mixed for five minutes using a hand-drill fitted with a plastic impeller. Further, the epoxy/CB mixture was put into the fiber impregnation bath and heated to 71°C. The mixture was heated to reduce viscosity for rapid fiber impregnation and bubble removal. The roving was fed through the resin bath and wound onto a cylindrical aluminum mandrel in three layers, each with a ±55° helical fiber orientation relative to the long axis of the mandrel and a pattern count of two. After winding, one layer of polyester peel ply was spirally wrapped around the mandrel with 50% overlap followed by one spiral layer of shrink tape with 75% overlap (Hi-Shrink, Dunstone, Charlotte, North Carolina). After the winding process, the tube was cured at 121°C for 1 h followed by 177°C for 3.5 h. After curing, the tube was removed from the mandrel and the rough ends were trimmed using a water-cooled diamond saw. The dimensions of the tube were 860 mm long, 63.5 mm inside diameter, and 1.35 mm wall thickness. Based on process conditions, the fiber volume fraction is estimated as 0.54.

4. ELECTRICAL IMPEDANCE TOMOGRAPHY

4.1 Introduction

EIT is a method for imaging the internal conductivity of a domain by boundary voltage measurements. EIT is attractive as an SHM modality because it is low cost and minimally invasive. Owing to the piezoresistive property of nanocomposites, mechanical strain or damage causes a local change in conductivity which can be imaged via EIT.

Mathematically, conductivity reconstructions are obtained by minimizing the difference between a vector of experimentally measured voltages and a vector of voltages predicted from a numerical model. The domain to be images is first lined with electrodes on the edges to carry out EIT. For the cylindrical specimen under study, current is injected from an electrode on the top edge to the electrode directly below it on the bottom edge (top-down injection scheme). This current injection pattern was chosen with the motivation that current needs to intercept the damage to substantiate a voltage change. For one particular injection, voltages are measured between adjacent electrode pairs on the same edge. This current injection and voltage measurement pattern is repeated until every top down pair receives a current injection. This voltage measurements scheme ensures that there is no mirroring of damage. Choosing a voltage measurement scheme similar to the injection scheme (as is common in most EIT reconstruction problems and literature) results in what is called as "ghosting" of damage. Owing to the symmetry of the cylinder a top-down voltage measurement scheme causes the reconstruction to show the presence of damages symmetric to the plane perpendicular to the cylinder axis. Thus, it is the author's recommendation to change voltage measurement schemes in accordance with the geometry at hand to circumvent such issues. The current injection and voltage measurement scheme is shown in Figure (4.1)

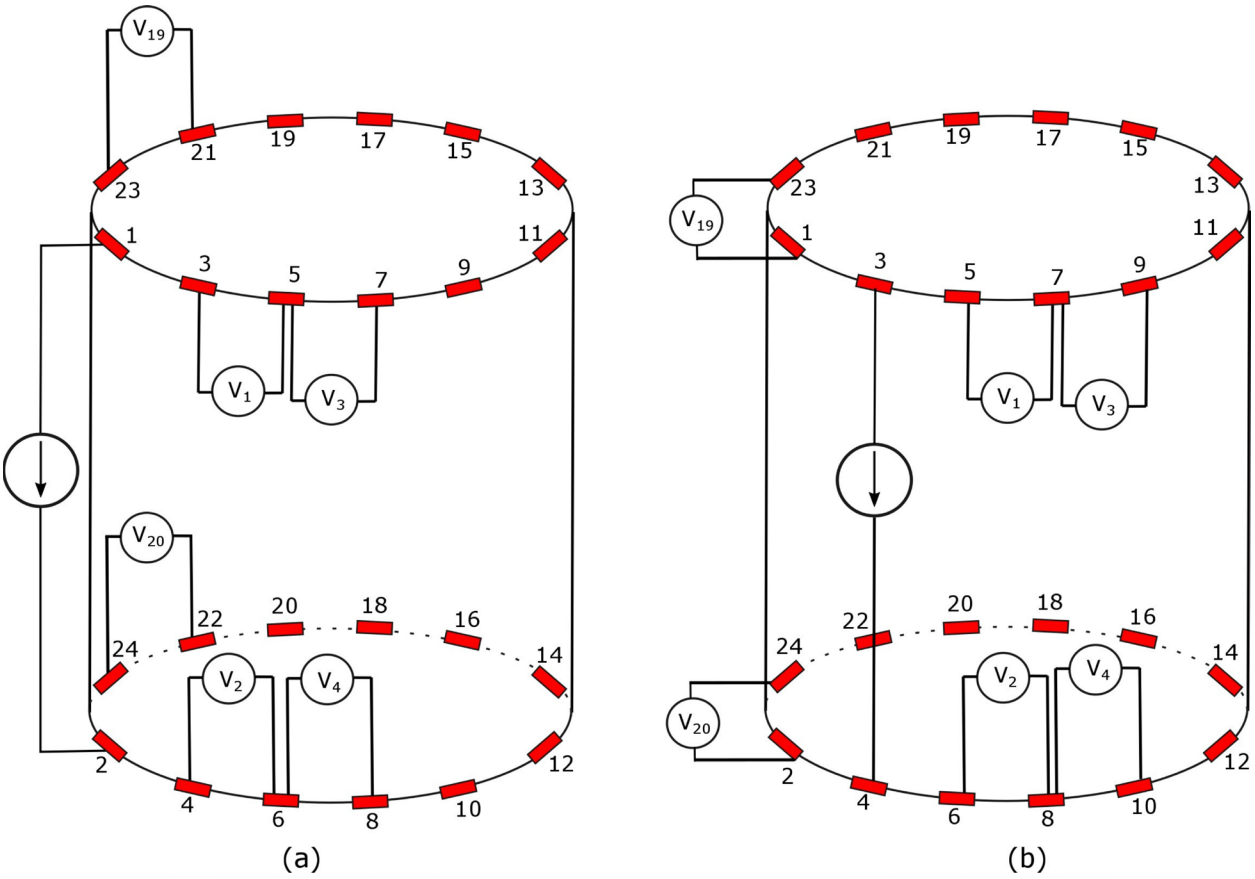

Figure 4.1: Schematic showing the current injection and voltage measurement schemes. Left: The first current injection. Right: The second current injection. The red rectangles indicate the electrodes.

The same current injection and voltage measurement scheme is used for the numerical model. As mentioned previously, the goal of EIT is mathematically achieved by a minimization procedure, which requires a voltage vector predicted by a numerical model. The procedure of predicting the boundary voltages numerically is called the forward problem. In the following sections the forward problem and the inverse problem will be treated individually to have an understanding of EIT. Note that anisotropic conductivity is not addressed in this work.

The specimen was manufactured by Jeffrey Kim and Dr. Charles. E. Bakis at Pennsylvania State University as part of a collaborative project.

4.2 Forward Problem

The forward operator is an integral part of predicting conductivity distribution inside a domain via EIT. $\boldsymbol{F}(\sigma)$, which denoted the forward operator, returns a vector of boundary voltages based on the conductivity distribution, σ, inside the domain and the applied current. Laplace's equation governs the relationship between current and voltages inside a domain, in the absence of an internal current source, which is shown in equation (4.1)

$$\boldsymbol{\nabla} \cdot \sigma \boldsymbol{\nabla} \phi = 0 \tag{4.1}$$

In equation (4.1), ϕ is the domain potential. To simulate the presence of contact impedance in the model, the complete electrode model employs boundary conditions as shown in equation (4.2).

$$\phi + z_l \sigma \boldsymbol{\nabla} \phi \cdot \boldsymbol{n} = V_l \tag{4.2}$$

Conservation of charge is enforced through equation (4.3) to maintain current entering the electrodes is equal to the current leaving the electrodes.

$$\sum_{l=1}^{L} \int_{S_l} \sigma \boldsymbol{\nabla} \phi \cdot \boldsymbol{n} \, \mathrm{d}S_l = 0 \tag{4.3}$$

In equations (4.2) and (4.3), $\boldsymbol{n}$ is an outward pointing normal vector, z_l is the contact impedance between the *l*th electrode and the domain, S_l is the area of the *l*th electrode, V_l is the voltage of the *l*th electrode, and L is the total number of electrodes. These equations are conveniently solved using the finite element method as shown in equations (4.4-4.8)

$$\begin{bmatrix} \boldsymbol{A}_M + \boldsymbol{A}_Z & \boldsymbol{A}_W \\ \boldsymbol{A}_W^T & \boldsymbol{A}_D \end{bmatrix} \begin{bmatrix} \boldsymbol{\Phi} \\ \boldsymbol{V}_e \end{bmatrix} = \begin{bmatrix} \boldsymbol{0} \\ \boldsymbol{I} \end{bmatrix} \tag{4.4}$$

$$A^e_{m\,ij} = \int_{\Omega_e} \frac{\partial w_i}{\partial x_k} \sigma_{kl} \frac{\partial w_j}{\partial x_l}\, \mathrm{d}\Omega_e \tag{4.5}$$

$$A_{Z\,ij} = \sum_{l=1}^{L} \int_{S_l} \frac{1}{z_l} w_i w_j\, \mathrm{d}S_l \tag{4.6}$$

$$A_{W\,li} = -\int_{S_l} \frac{1}{z_l} w_i\, \mathrm{d}S_l \tag{4.7}$$

$$A_D = \mathrm{diag}\left(\frac{S_l}{z_l}\right) \tag{4.8}$$

In the preceding, $\boldsymbol{\Phi}$ is the vector of domain potentials, $\boldsymbol{V_e}$ is a vector of electrode voltages, and $\boldsymbol{I}$ is the vector of current injections. The *ij*th entry of the local diffusion stiffness matrix for the *e*th element is formed as shown in equation (4.5) where w_i is the *i*th basis function. For the work herein presented, the domain was discretized using three-dimensional tetrahedral elements. A sufficient number of elements were used to capture the domain curvature. Linear interpolation functions are used with $w_1 = \zeta_1$, $w_2 = \zeta_2$, $w_3 = \zeta_3$ and $w_4 = 1 - \zeta_1 - \zeta_2 - \zeta_3$. Two dimensional shape functions are used for integration over the electrode area. The shape functions used for the electrodes are $w_1 = \zeta_1, w_2 = \zeta_2$ and $w_3 = 1 - \zeta_1 - \zeta_2$. Here, it is important to note that the forward problem can solved by any suitable form of discretization.

4.3 Inverse Problem

The inverse problem is a topic that has received much attention from a mathematical point of view [62]–[64]. Being an ill-posed inverse problem, many methods have been proposed to mathematically attain the best possible solution. Although many methods are available, the author here treats one method in depth: a one-step linearization employing a damped least-squares formulation. The author has used the one step linearization for experimental reconstructions. However, the Gauss-Newton method has also proven to be an efficient method of conductivity reconstruction in EIT [50], [51]. Steps for the Gauss-Newton method are outlined in appendix B.

4.3.1 Difference Imaging via One Step Linearization

Having formulated the forward problem, we can now formulate the inverse problem. The inverse problem in simple mathematical terms is expressed as in equation (4.9).

$$\min(\|\boldsymbol{W} - \boldsymbol{V}_m\|_2^2) \tag{4.9}$$

To elucidate the meaning of equation (4.9), $\boldsymbol{W}$ is a vector of numerically predicted voltage data (i.e. voltage predicted by the forward model) and $\boldsymbol{V_m}$ is a vector of experimentally measured voltage data. Difference imaging employs the measurement of voltage data before and after damage occurs in a structure. Let $\boldsymbol{V}(t_1)$ represent a vector of voltage data taken before any sort of damage occurs and let $\boldsymbol{V}(t_2)$ be a vector of voltage data taken after the occurrence of damage. Then $\boldsymbol{V}_m$ is given by equation (4.10).

$$\boldsymbol{V}_m = \boldsymbol{V}(t_2) - \boldsymbol{V}(t_1) \tag{4.10}$$

Here the vector of experimentally measure voltages, $\boldsymbol{V}(t_1)$ is called the baseline state. Difference imaging is necessary since the finite element model is not completely representative of the actual specimen under study. The most common sources of error are the placement of electrodes and the domain shape. In our case, the domain is curved and consequently the application of evenly spaced electrodes is even more challenging. Thus these common errors are cancelled out in difference

imaging. $\boldsymbol{W}$ represents a similar set of voltage differences, however it is expressed as shown in equation (4.11).

$$\boldsymbol{W} = \boldsymbol{F}(\boldsymbol{\sigma}_2) - \boldsymbol{F}(\boldsymbol{\sigma}_1) \tag{4.11}$$

Recollect, from the previous section that $\boldsymbol{F}(\boldsymbol{\sigma})$ is the solution to the forward problem. However, notice that $\boldsymbol{\sigma}$ is boldfaced in anticipation of the discretization via the finite element method. Now to proceed solving the inverse problem, $\boldsymbol{F}(\boldsymbol{\sigma})$ is approximated by a Taylor series expansion centered about an initial conductivity estimate $\boldsymbol{\sigma_0}$. Only the linear terms are retained as shown in equation (4.12 and 4.13).

$$\boldsymbol{F}(\boldsymbol{\sigma}_1) \approx \boldsymbol{F}(\boldsymbol{\sigma_0}) + \frac{\partial \boldsymbol{F}(\boldsymbol{\sigma_0})}{\partial \boldsymbol{\sigma}}(\boldsymbol{\sigma}_1 - \boldsymbol{\sigma}_0) \tag{4.12}$$

$$\boldsymbol{F}(\boldsymbol{\sigma}_2) \approx \boldsymbol{F}(\boldsymbol{\sigma}_0) + \frac{\partial \boldsymbol{F}(\boldsymbol{\sigma_0})}{\partial \boldsymbol{\sigma}}(\boldsymbol{\sigma}_2 - \boldsymbol{\sigma}_0) \tag{4.13}$$

By substituting equations (4.12) and (4.13) into the expression for $\boldsymbol{W}$, we have the expression as shown in equation (4.14).

$$\boldsymbol{W} \approx \frac{\partial \boldsymbol{F}(\boldsymbol{\sigma_0})}{\partial \boldsymbol{\sigma}}(\boldsymbol{\sigma_2} - \boldsymbol{\sigma_1}) \tag{4.14}$$

Now, by rewriting $\boldsymbol{J} = \partial \boldsymbol{F}(\boldsymbol{\sigma_0})/\partial \boldsymbol{\sigma}$ and defining $\Delta\boldsymbol{\sigma} = \boldsymbol{\sigma}_2 - \boldsymbol{\sigma}_1$, we rewrite equation (4.14) as shown in equation (4.15).

$$\boldsymbol{W} \approx \boldsymbol{J}\Delta\boldsymbol{\sigma} \tag{4.15}$$

Equation (4.15) is now used to form the minimization problem as shown in equation (4.16).

$$\Delta\boldsymbol{\sigma}^* = \min_{-1.01\boldsymbol{\sigma_0} < \Delta\boldsymbol{\sigma} < 0.01\boldsymbol{\sigma_0}} \left(\left\| \begin{bmatrix} \boldsymbol{J} \\ \alpha \boldsymbol{L} \end{bmatrix} \Delta\boldsymbol{\sigma} - \begin{bmatrix} \boldsymbol{V_m} \\ \boldsymbol{0} \end{bmatrix} \right\|_2^2 \right) \tag{4.16}$$

There are several important differences between equation (4.16) and equation (4.9). First $\Delta\boldsymbol{\sigma}^*$ is the conductivity change from time t_1 to t_2 which satisfies the minimization problem. Second, the minimization is written in the form of a damped least squares solution. The EIT inverse problem being underdetermined and ill-posed requires regularization in order to obtain reasonable conductivity changes. Additionally, regularization has been added in the form of $\boldsymbol{L}$. Here, we choose the discrete Laplace operator as the regularization matrix.

$$\boldsymbol{L} = L_{ij} = \begin{cases} \text{degree } (\Omega_e) & \text{if i = j} \\ -1 & \text{if i} \neq \text{j and } \Omega_e \text{ is adjacent to } \Omega_i \\ 0 & \text{otherwise} \end{cases} \tag{4.17}$$

L_{ij} is a square matrix which has dimensions equal to the number of elements in the finite element mesh of the forward problem. The ith value of the diagonal of the regularization matrix is equal to the number of elements surrounding the ith element. An element is said to surround a particular element when an element shares an edge with another element in two dimensions and shares a face with another element is three dimensions. If the ith and jth elements share an edge then the entry $L_{ij} = L_{ji} = -1$. To further elucidate the formation of L, we look at Figure (4.2). We consider a triangular mesh as an example. Element i shares an edge with three other elements namely j, k and l. Following the explanation, the entry $L_{ii} = 3$ (the diagonal entry) and the entry $L_{ij} = L_{ji} = L_{ik} = L_{ki} = L_{il} = L_{li} = -1$. Figure (4.2) does not shows a complete mesh but only serves the purpose in clarifying how the regularization matrix is formed.

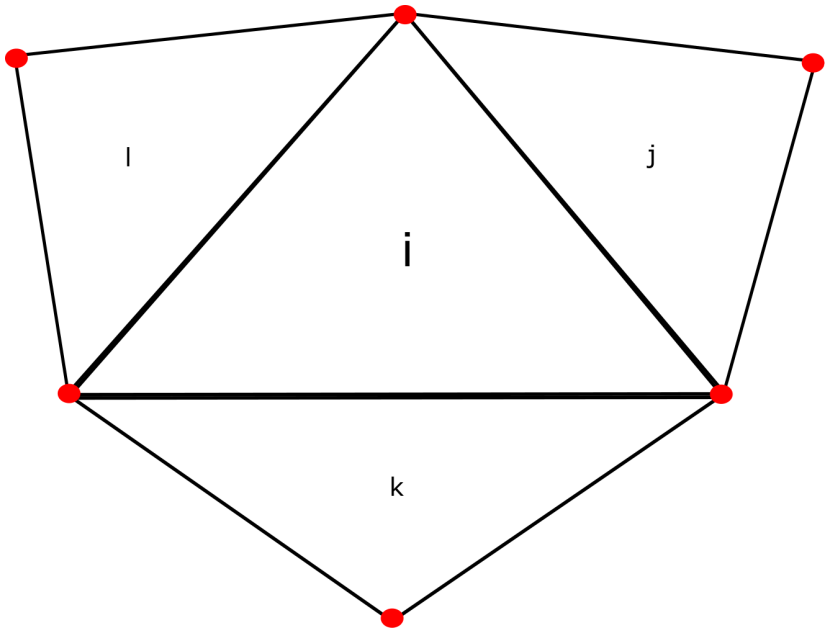

Figure 4.2: Schematic showing an example of forming the regularization matrix

Returning to equation (4.16), α is known as the regularization parameter and controls the contribution of the regularization matrix previously discussed. Next, $\boldsymbol{J}$ is known as the sensitivity matrix. Derivation of a closed-form for this derivative is rigorously treated by Holder [65]. Nonetheless, the final result is shown in equation (4.18). This lets us relate the electrode voltage perturbations to conductivity perturbations.

$$J_{MN\,e} = -\int_{\Omega_e} \frac{\partial u^M}{\partial x_i}\frac{\partial u^N}{\partial x_i} d\Omega_e \tag{4.18}$$

Computationally, $\boldsymbol{J}$ is defined as the contraction of the gradient of the voltage on the eth element due to the current injection on the Mth electrode pair and the gradient of the voltage on the eth element due to the Nth adjoint field. The integral is evaluated over the eth element. This integral can be thought as the sensitivity of the Nth electrode measurement pair due to slight conductivity perturbation of the eth element while current is injected in the Mth electrode pair.

And lastly, note that the conductivity change in equation (4.16) is bounded. This bound is physically motivated. That is, damage causes a conductivity loss thereby necessitating that $\Delta\boldsymbol{\sigma}$ be

negative and no more than a 100% loss. However, a 'wiggle room' of ±1% is added to these bounds to accommodate noise in the measurements.

4.4 Calibrating the forward model

An important part of reconstructing the conductivity change via the one step linearization is choosing the right $\boldsymbol{\sigma_0}$ to carry out the linearization. This conductivity is chosen by using information from the pre-damaged voltage data. Figure (4.3) shows the comparison between the forward model and the pre-damaged voltage data for a tube with length-to-diameter ratio of 2:1

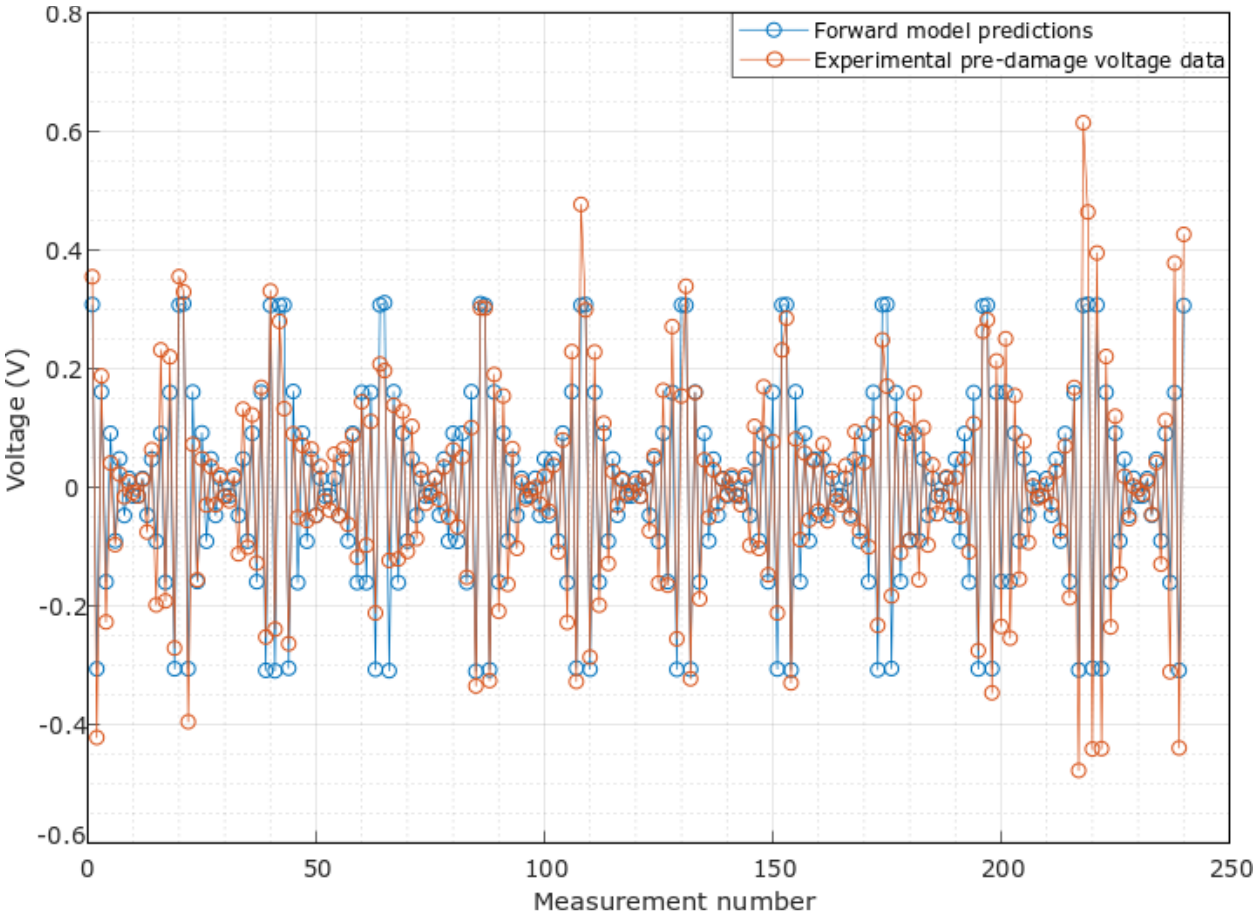

Figure 4.3: Plot comparing the forward model predictions to the undamaged voltage state in a 2:1 length-to-diameter tube

A baseline conductivity of 0.9×10^{-3} S/m was chosen as σ_0. The baseline conductivity was chosen by comparing the L_2 norm of the error vector for different baseline conductivities. The error vector is defined as the difference between the forward predicted voltages and the experimental pre-damage voltage data. The L_2 norm of the error vector using 0.9×10^{-3} S/m as the baseline conductivity was 0.93, whereas the L_2 norm of the error vector using 0.8×10^{-3} S/m and 1×10^{-3} S/m as the baseline conductivity were 0.97 and 0.98 respectively. As evident from Figure (4.3) the forward model does follow the experimental data quite closely. The baseline conductivity thus calibrated will be used for all specimens in this study irrespective of their lengths since they were cut out from the same longer tube. Here it is also worth commenting on the number of measurements and the trend followed by the voltage data. The data plotted in Figure (4.3) shows voltage difference measurements for 12 top-down injection pairs. Since the setup used is a 24 electrode setup there are 24 voltage difference measurements for each injection. However, the voltage difference measurements involving the current driving electrodes are removed since even a slight error in contact impedance can cause a large variation in conductivity reconstruction. Thus, for each injection, there are 20 usable voltage differences and a total of 240 measurements for 12 top-bottom injections.

The trend followed by the voltage differences is a consequence of the geometry involved. As shown in Figure (4.4), we see that the magnitude of voltage difference decreases as we move away from the driving electrodes (where current is injected) and the magnitude reaches a minimum at a position diametrically opposite the current injected electrode pair.

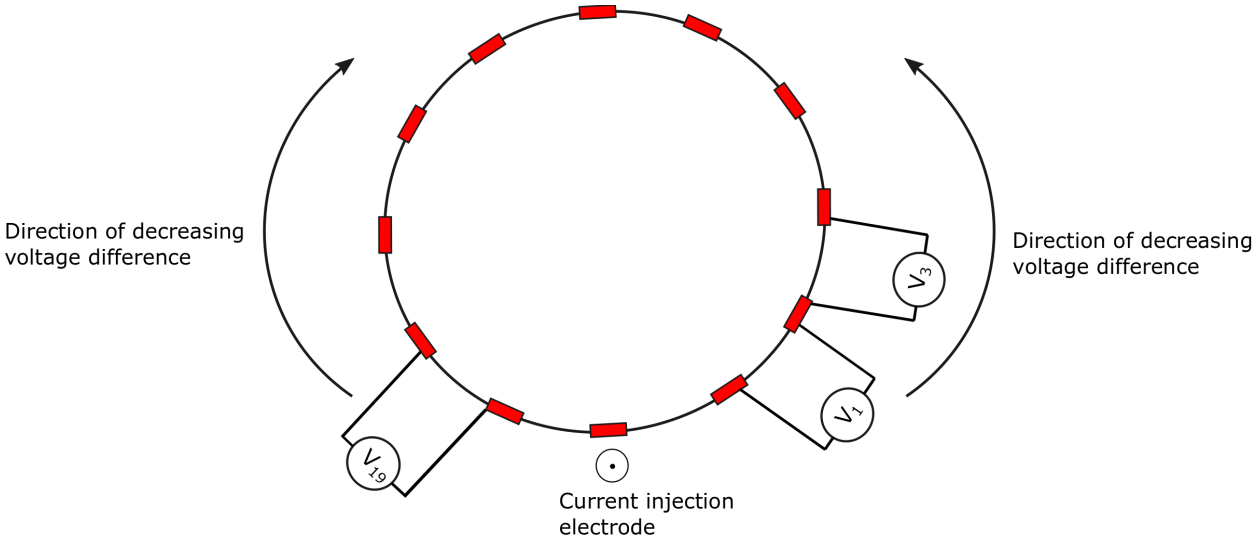

Figure 4.4: Schematic showing the direction of decreasing voltage difference for a current injection. The schematic shows the top view of the cylinder.

5. EXPERIMENTAL DAMAGE DETECTION IN GF/EPOXY TUBES VIA ELECTRICAL IMPEDANCE TOMOGRAPHY

Having discussed the mathematical framework of EIT, this chapter will look at experimental damage detection in a glass fiber/epoxy tube with CB filler. This chapter will be organized as follows. First, the experimental setup for damage detection will be shown. Second, through-hole damage detection and sensitivity study to multiple damage will be discussed. Finally, detection of barely visible impact damage (BVID) will be discussed.

5.1 Experimental Setup

Here the general experimental procedures for damage detection are discussed. The long tube, provided by our collaborators at Penn State, was cut to sizes of appropriate length, which will be discussed in the following sections. The tube was cut with a water-cooled tile saw. After cutting the tube, electrodes were attached to the edges of the specimen. To do so, the edges were lightly sanded with fine-grit sand paper and cleaned with acetone. Cleaning with acetone is an important process since this removes dirt and other contaminants which could otherwise cause an increase in contact impedance. Colloidal silver paint was applied on either edges of the cylindrical specimen with the aid of a 3D-printed spacer tool. The 3D printed spacer tool is vital in this process for uniform spacing of the electrodes to minimize the error between the forward model and the experimental specimen. After applying the silver paste, copper tape electrodes were applied over the painted silver surface. This is shown in Figure (5.1),

Next, acrylic sheets were placed on both ends of the cylinder and more copper tape was attached over the surface of the sheets connecting the copper tape placed over the edges of the electrodes. The acrylic sheets were used in this case to prevent directly attaching alligator clips to the surface of the electrodes. Directly attaching the alligator clips over the copper tape on the edges of the electrodes could rip the electrodes off the specimen. This might initiate the need of re-attaching the electrodes which could cause additional errors between the finite element model and the experiment. Also, Figure (5.1) shows masking tape attached to the tube. The masking tape prevents direct contact between the copper electrodes and the specimen. The finite element model simulates

current injected from the top edge to the bottom edge and does not account for current injected through the surface of the tube. Hence the masking tape is a method of assuring good correlation between the finite element model and the actual experimental setup.

Figure 5.1: Specimen of length-to-diameter ratio 2:1 prepared for EIT. The copper electrodes are attached over a layer of masking tape to prevent current being injected through the sides. This ensures good correspondence with the forward model.

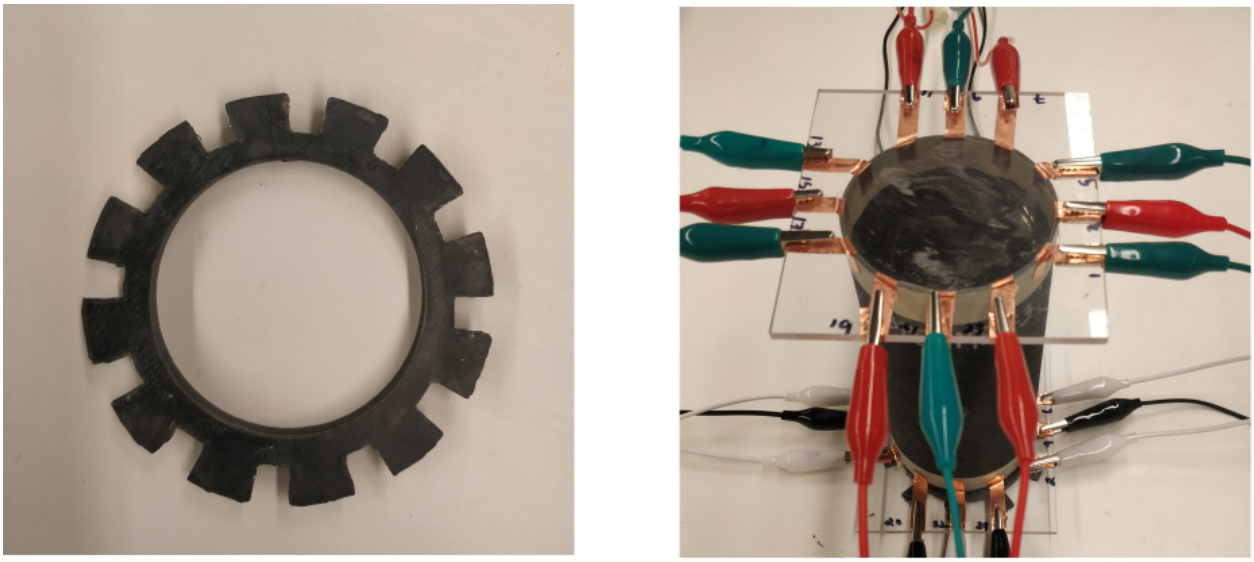

(a) (b)

Figure 5.2: (a) 3D-printed spacing tool used to attach copper electrodes at regular intervals on the specimen edges (b) Specimen with electrodes attached to acrylic sheets and prepared for EIT.

Direct currents (DC) were injected into the 24-electrode setup by a Keithley 6221 high-precision current source, and voltages were measured with National Instruments PXIe-6368 data acquisition (DAQ) cards. Current magnitudes were selected to result in voltages within the DAQ's 10 V range. The current magnitude to be injected was determined by first using four-point measurements to determine the highest resistance between top-bottom electrode pairs. Since the same magnitude of current will be injected in the undamaged and damaged state, it is important to account for a marginal increase in resistance caused by the introduction of damage. Hence, while choosing the current to be injected through the specimen, instead of pushing the DAQ to its limit of 10V, a maximum voltage of approximately 6V was chosen. A sample measurement is shown in Figure (5.3). Data is collected at 200 Hz for 5 seconds. This is done twice to make sure there is no drift in voltage measurement with time. It is important to attain good steady data on electrode voltages, which could otherwise indicate variable contact impedance between the specimen and the electrode. It is vital to make sure contact impedance does not change over time since the finite element model assumes a constant, minimal contact impedance between the electrodes and the specimen.

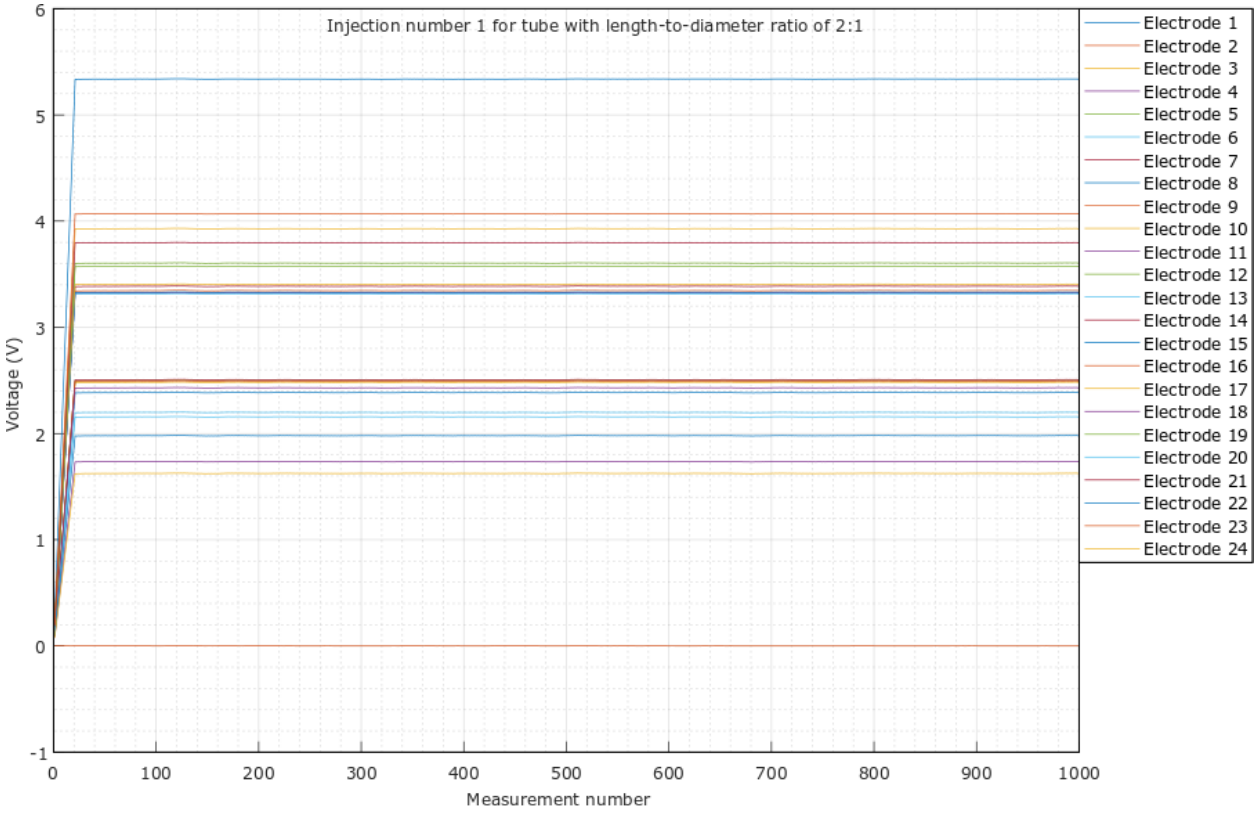

Figure 5.3: Plot showing electrode voltage data collected from the DAQ for current injection 1 for the tube with length-to-diameter ratio of 2:1

5.2 Through-hole damage detection

The lower threshold of damage detection is an important aspect in SHM. In order to understand the lower threshold of detectable damage, a sensitivity study is carried out. The sensitivity study is performed by considering through holes of varying sizes, at multiple locations, and on tubes of varying length. The first specimen cut has a length-to-diameter ratio of 2:1. Voltage is collected prior to introduction of any damage and is used as the baseline voltage. The first hole, of diameter 4.76 mm, was drilled near the center of the specimen. It is important to note that the holes were drilled without any internal backup thereby causing some exit hole splintering. However, the change in conductivity due to the hole is expected to be much larger than the splintering damage thereby overshadowing the change in conductivity caused by exit hole splintering. The 4.76 mm hole was subsequently bored out to larger diameters of 7.94 and 9.53 mm. EIT measurements were taken after the introduction of each hole. This procedure of drilling a hole 4.76 mm diameter and

boring it to larger diameters was carried out for two others locations, each at varying distances from the edge of the tube. The locations of the holes are shown in Figure (5.5)

Figure 5.4: Occurrence of splintering damage. Splintering damage occurred because the holes were drilled without any backup

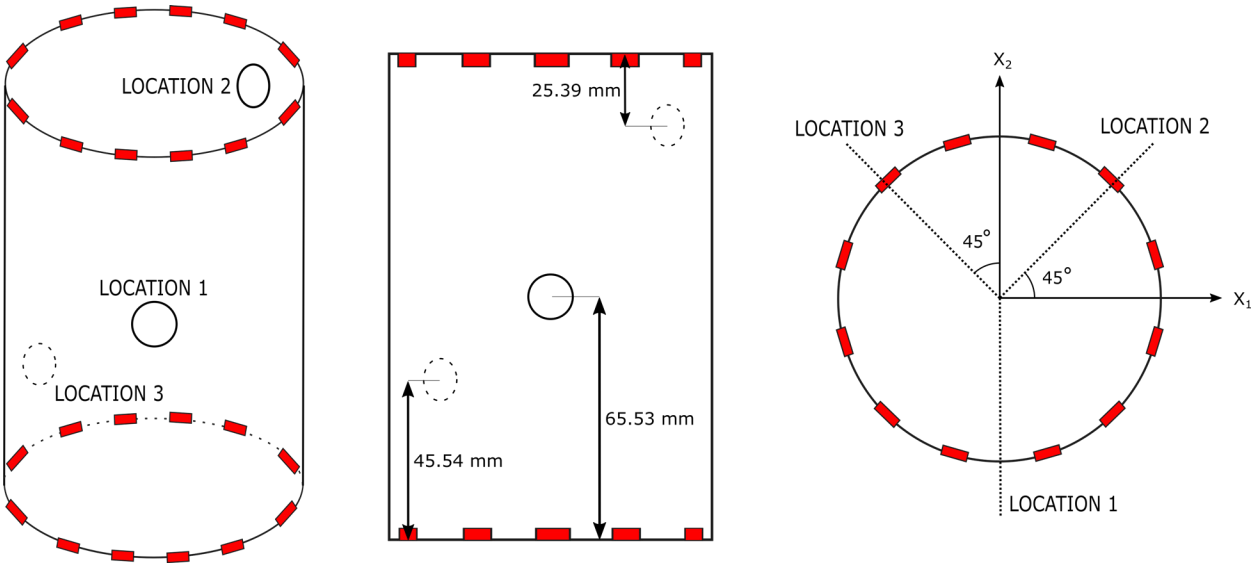

Figure 5.5: Schematic showing through-hole locations on the 2:1 specimen. Left: Tube as viewed from an angle. Middle: Hole locations along the tube's axis. Right: Hole locations in the circumferential direction. Note that solid lines are used when the hole is visible from the current line of sight and dashed lines are used when the hole is not visible from the current line of sight.

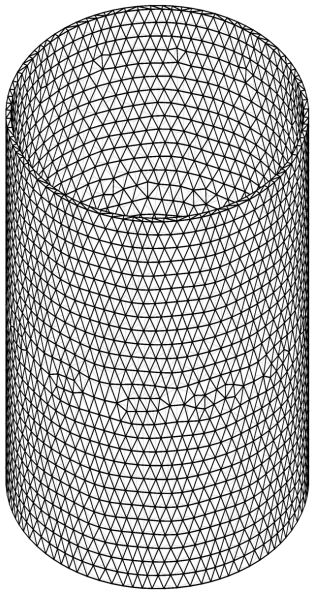

Figure 5.6: Mesh used for EIT reconstruction.

The EIT reconstruction results are shown in Figure (5.7). The mesh used for reconstruction is shown in Figure (5.6). The EIT reconstructions show the percentage change in conductivity due to the through-holes. We can make several interesting observations from the conductivity reconstructions. First, EIT fails to detect any holes near the center of the specimen, i.e. at location 1. This is evident in the first row of Figure (5.7) where there is no visible conductivity change. Second, EIT seemingly loses sensitivity to damage further away from the edges of the specimen where voltage is collected. This can be seen in the lower conductivity change magnitude at location 3 than location 2 for similar hole sizes. However, when the holes at location 3 are plotted on their own scale (by using voltage data corresponding to the largest hole at location 2 as the baseline), as shown Figure (5.8), damage-induced conductivity changes are clearly visible. And, third EIT fails to detect the hole of 4.76 mm at any location. This could indicate the lower threshold of detectability for a tube of this particular aspect ratio.

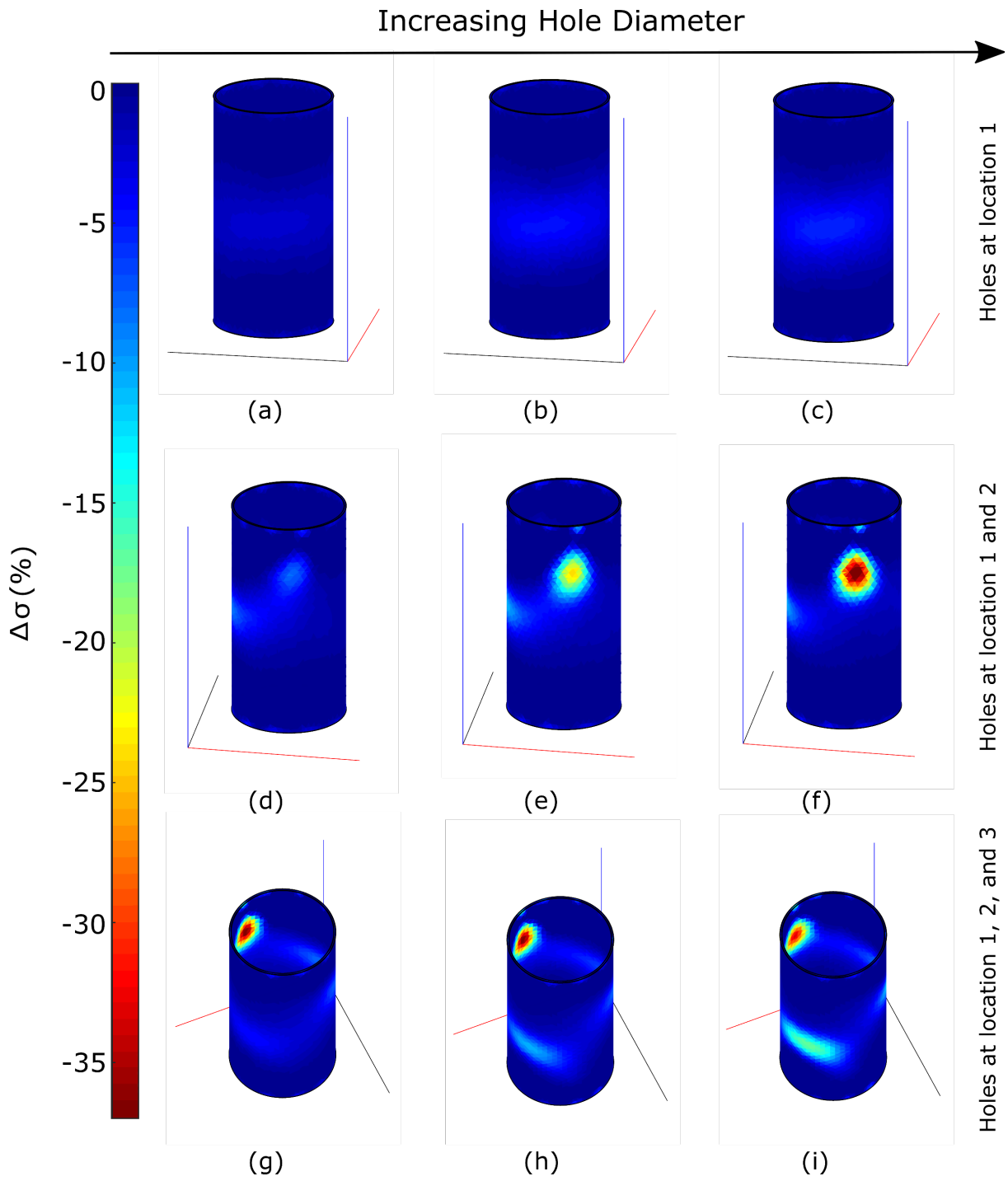

Figure 5.7: EIT reconstructions of (a) 4.76 mm hole at location 1 (b) 7.94 mm hole at location 1 (c) 9.53 mm hole at location 1 (d) 4.76 mm hole at location 2 (e) 7.94 mm hole at location 2 (f) 9.53 mm hole at location 2 (g) 4.76 mm hole at location 3 (h) 7.94 mm hole at location 3 (i) 9.53 mm hole at location. A colored triad is included to help orient the reader to rotations of the tube.

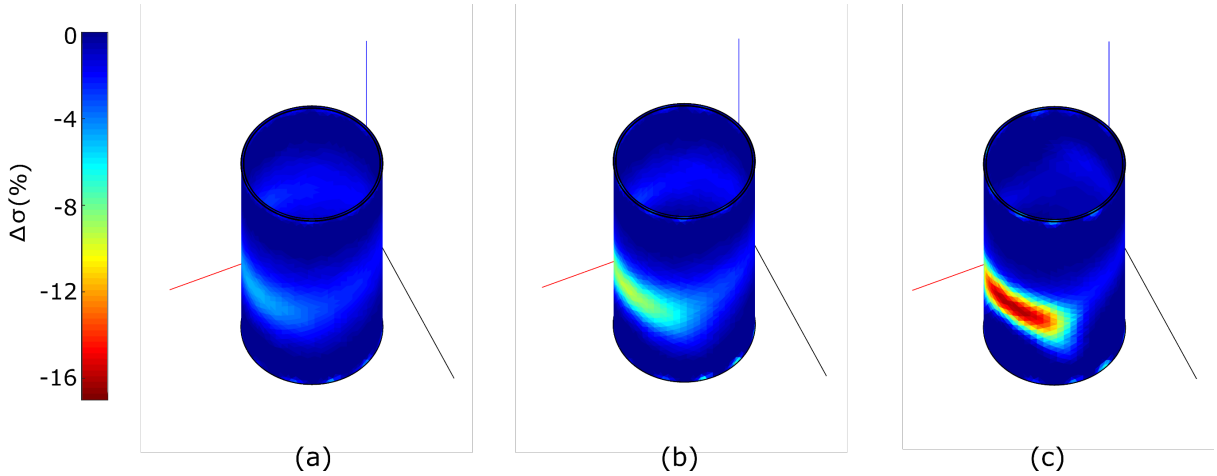

Figure 5.8: EIT reconstructions of holes at location 3. The damage state shown in Figure 5.7(f) is chosen as the baseline for these reconstructions.

To better understand the sensitivity of EIT with regard to tube aspect ratio, two more specimens were studied. One with a length-to-diameter ratio of 1:1 and another with a length-to-diameter ratio of 3:2. In both these specimens, a hole of diameter 4.76 mm was initially drilled out at the center of the tube which was subsequently bored out to 7.94 mm and 9.53 mm in diameter. Figure (5.9) shows the EIT reconstructions for the tube with length-to-diameter ratio of 1:1 and Figure (5.10) shows the tube with length-to-diameter ratio of 3:2. These results show that EIT is indeed able to capture damage near the center of the specimen on lower aspect ratio tubes. Further, EIT is clearly able to capture the 4.76 mm hole in the 1:1 specimen which previously went undetected. However, the hole of size 4.76 mm goes undetected in the tube with length-to-diameter ratio of 3:2.

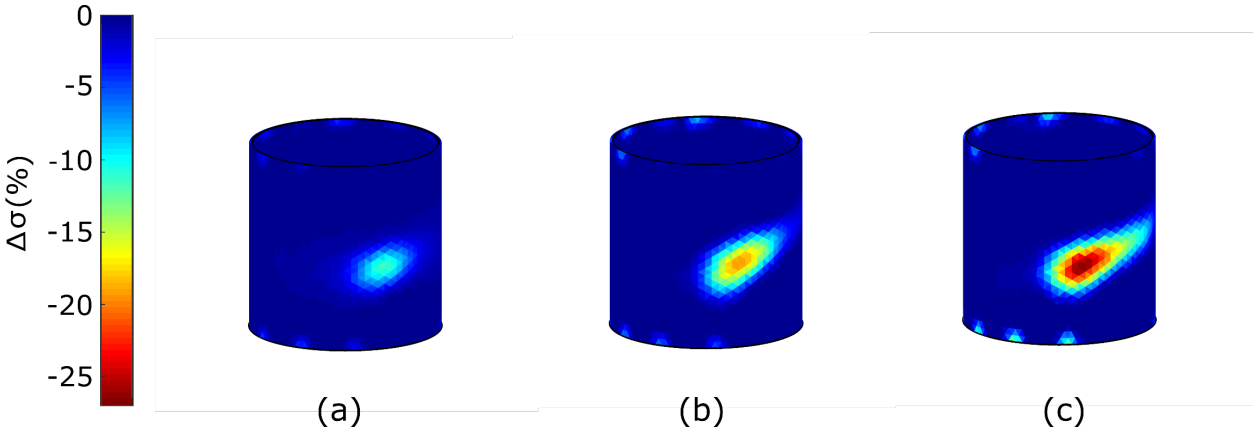

Figure 5.9: EIT reconstructions on the tube with length to diameter ratio of 1:1 (a) 4.76 mm hole (b) 7.94 mm hole (c) 9.53 mm hole.

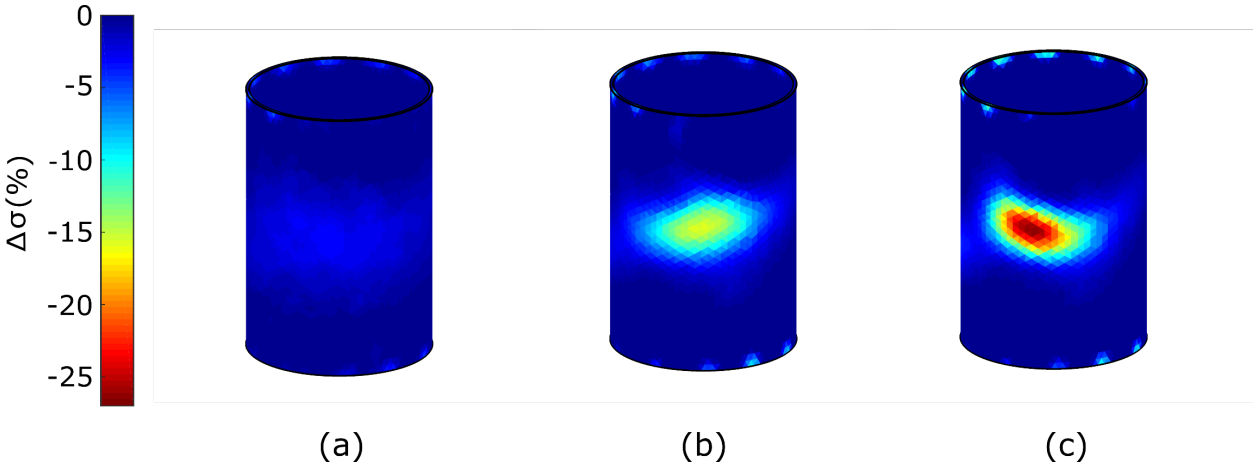

Figure 5.10: EIT reconstructions on the tube with length to diameter ratio of 3:2 (a) 4.76 mm hole (b) 7.94 mm hole (c) 9.53 mm hole.

While the EIT reconstructions provide information on the location and intensity of damage, it is also worthwhile to look into the voltage difference caused by the occurrence of damage. As discussed in the previous chapter, voltage difference is taken between the baseline state and the damaged state. The following plots shows some comparisons between holes of varying sizes at different locations and also shows comparisons of holes of same sizes at similar locations but for tubes of varying aspect ratio. This information gives us an insight into why EIT is unable to reconstruct some conductivity changes occurring due to damage.

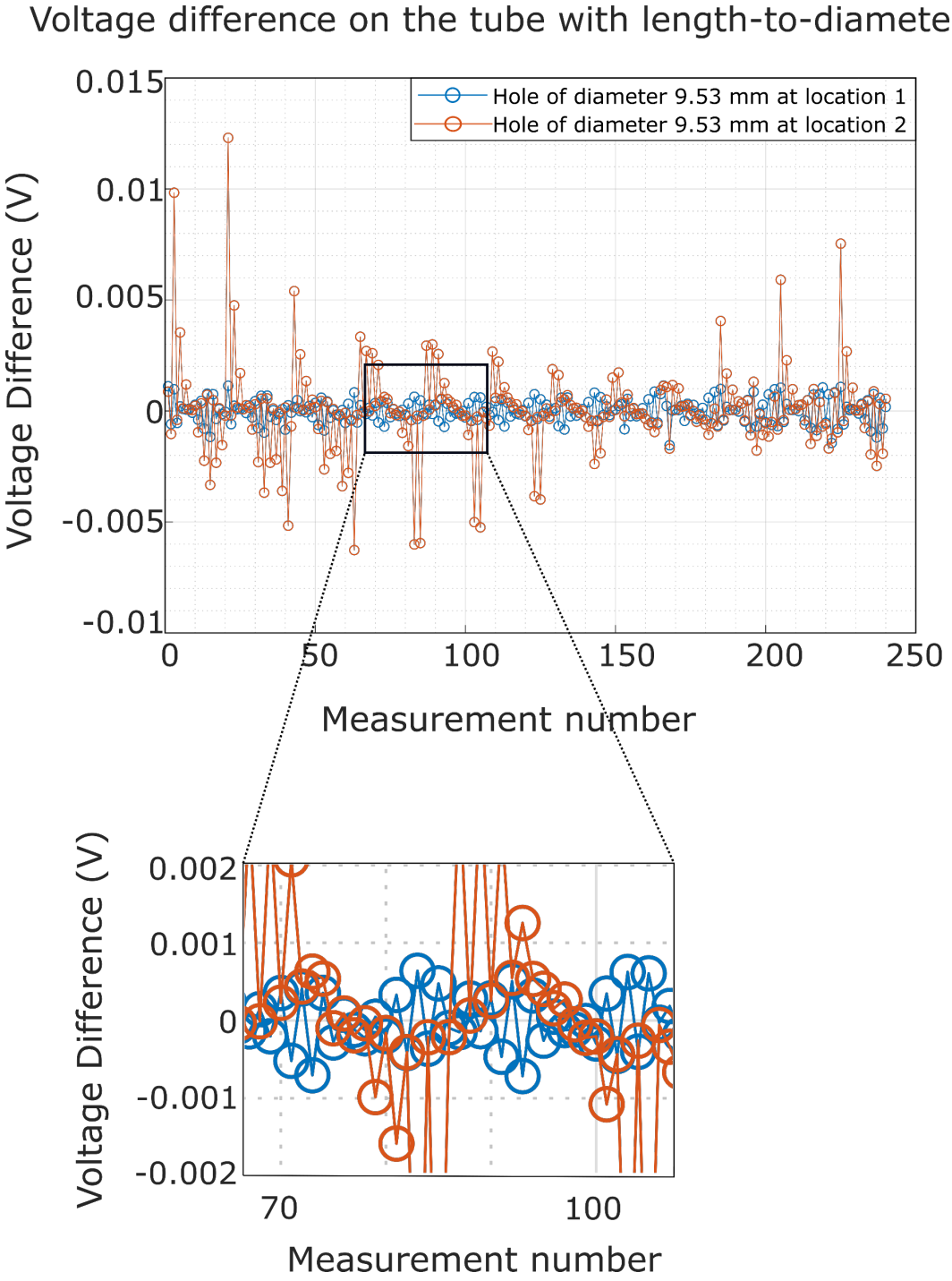

Figure 5.11: Voltage difference plots comparing a hole of size 9.53 mm at different locations on a tube of length-to-diameter ratio of 2:1

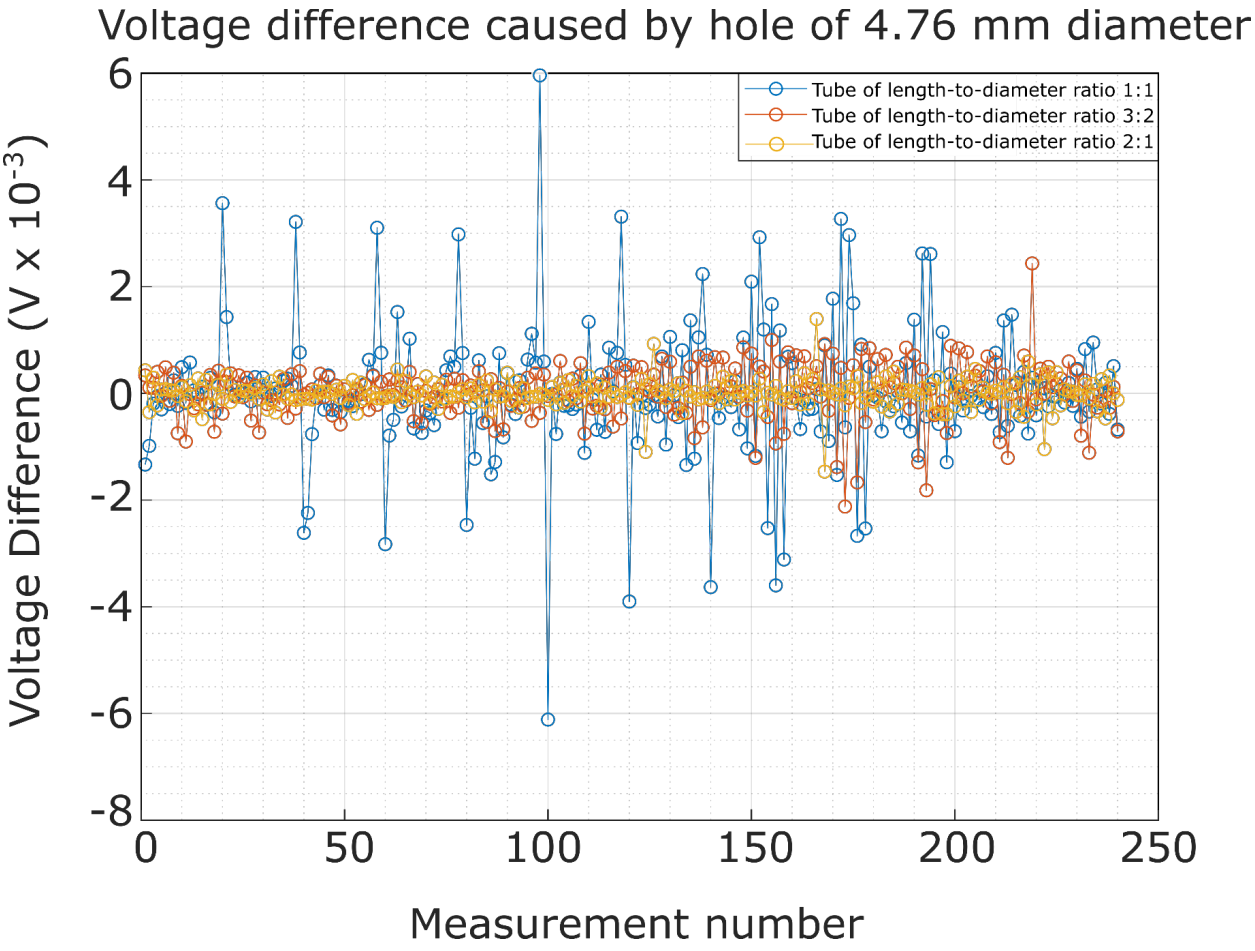

Figure 5.12: Voltage difference plots comparing a hole of size 4.76 mm for different aspect ratio tubes

Figure (5.11) shows the experimental voltage difference vectors for the hole of diameter 9.53 mm at location 1 and location 2 in the tube of length-to-diameter ratio of 2:1. The zoomed in portion of the plot in Figure (5.11) shows that that there is only a small voltage variation (close to 0) shown in blue which represents the damage data for the hole at location 1, whereas there is a considerable change in voltage caused by the hole at location 2 (shown in red). This implies that the magnitude of voltage difference caused by the hole at location 1 is insufficient to reconstruct any useful conductivity data, which explains why EIT fails to locate the hole at location 1. Similarly, looking at the plot in Figure (5.12), there are only small voltage differences caused by the hole of 4.76 mm for the tubes of length-to-diameter ratio of 3:2 and 2:1 compared to the voltage difference caused by the 4.76 mm hole for the tube with length-to-diameter ratio of 1:1.

5.3 Impact damage detection

BVID is an important consideration for composite structures. Low velocity impacts can cause sub-surface damage in the form of delamination and matrix cracking which could propagate under loading conditions and lead to catastrophic failure. To evaluate the capability of EIT to detect sub-surface damage caused by low-velocity impact, a tube of length-to-diameter ratio of 1:1 was cut. The impact experiment was conducted in a CEAST 9340 drop tower with a steel hemispherical indenter of 15.8 mm diameter. Since the machine fixture was built for testing plate specimens, an additional fixture was machined out of aluminum to fit the cylindrical specimen in the drop tower. The machined fixture is shown in Figure (5.13). The tube is snugly fit over the aluminum fixture to prevent the tube from collapsing inwards and the aluminum rod is securely fastened to the impact machine with the help of C-clamps. Two impacts, measuring 14 J and 10 J, were carried out on the same specimen at two circumferential locations approximately at the middle of the tube. The impacts resulted in BVID as shown in Figure (5.14)

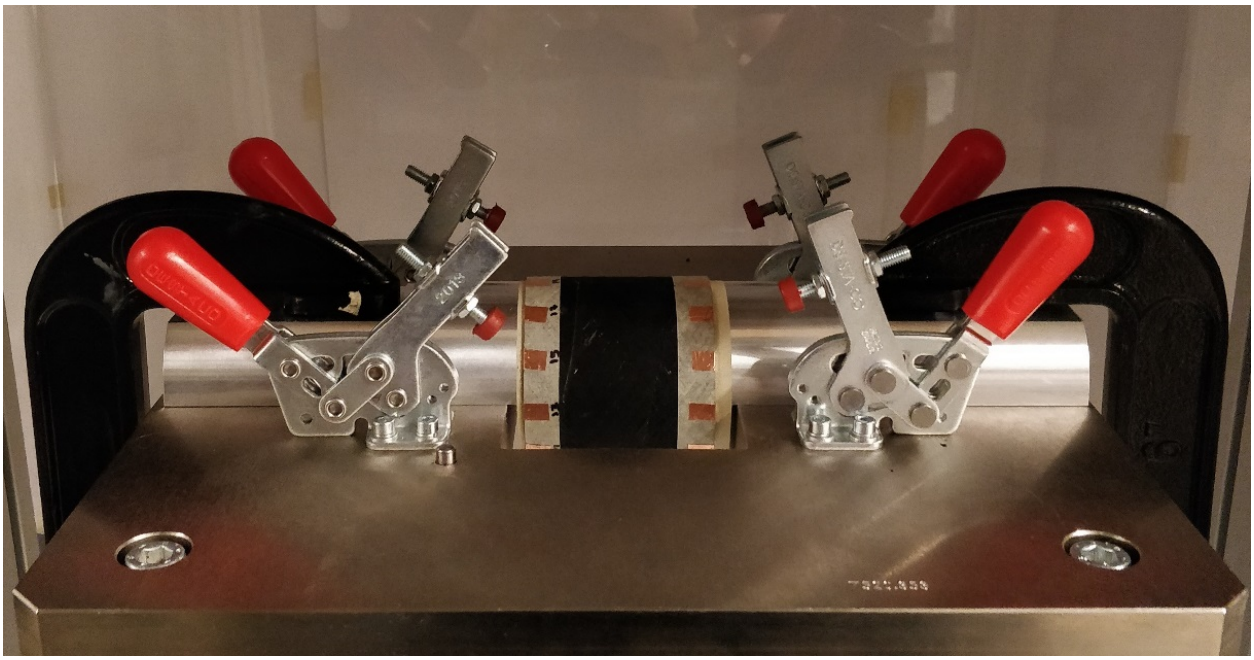

Figure 5.13: 1:1 specimen fit over an aluminum rod and secured via C-clamps within the drop tower for impact testing

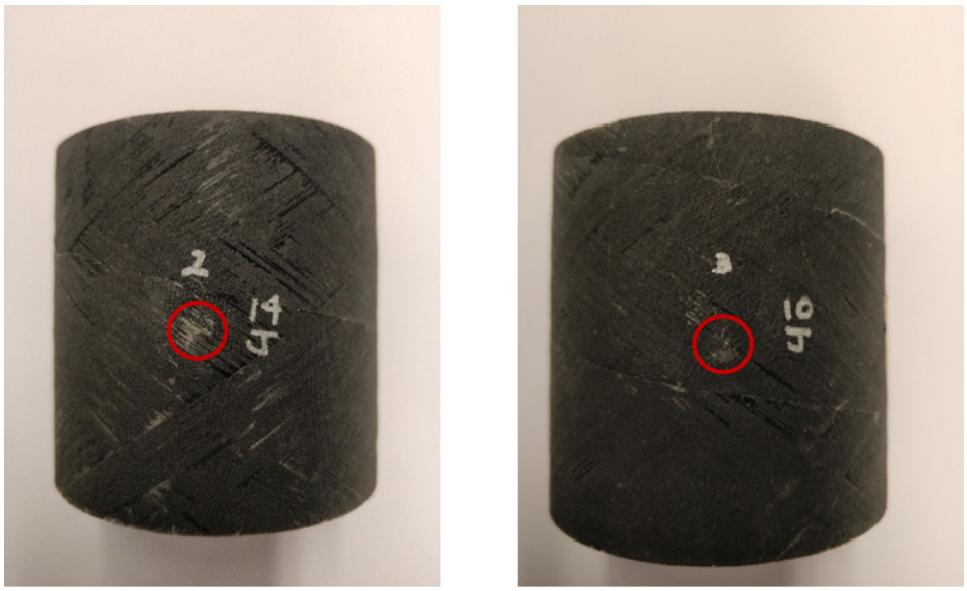

Figure 5.14: Post-impacted tube (a) 14 J (b) 10 J. Note that the impact damage is barely visible. The red circles indicate the impact locations.

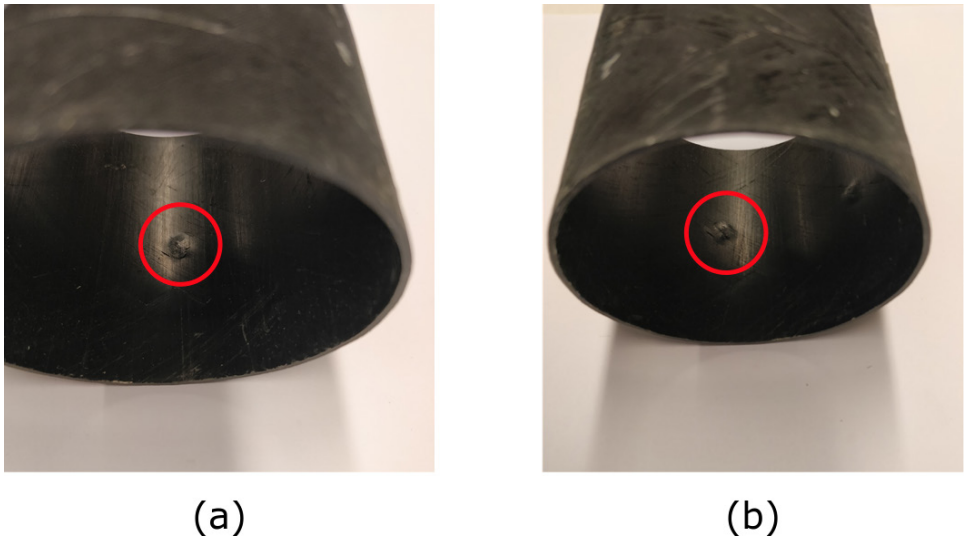

Figure 5.15: Rear side of post-impacted tube (a) 14 J (b) 10 J. The red circles indicate the impact locations.

The same 24 electrode setup used for through-hole damage detection was used impact damage detection. However, some electrodes were unresponsive after the impact and had to be reattached. This causes some additional errors in the conductivity reconstructions, since the baseline was taken

prior to impact. These errors seem to be minimal as good conductivity reconstructions are obtained as shown in Figure (5.16). Figure (5.17) shows the comparison of the conductivity reconstruction to the actual impact location.

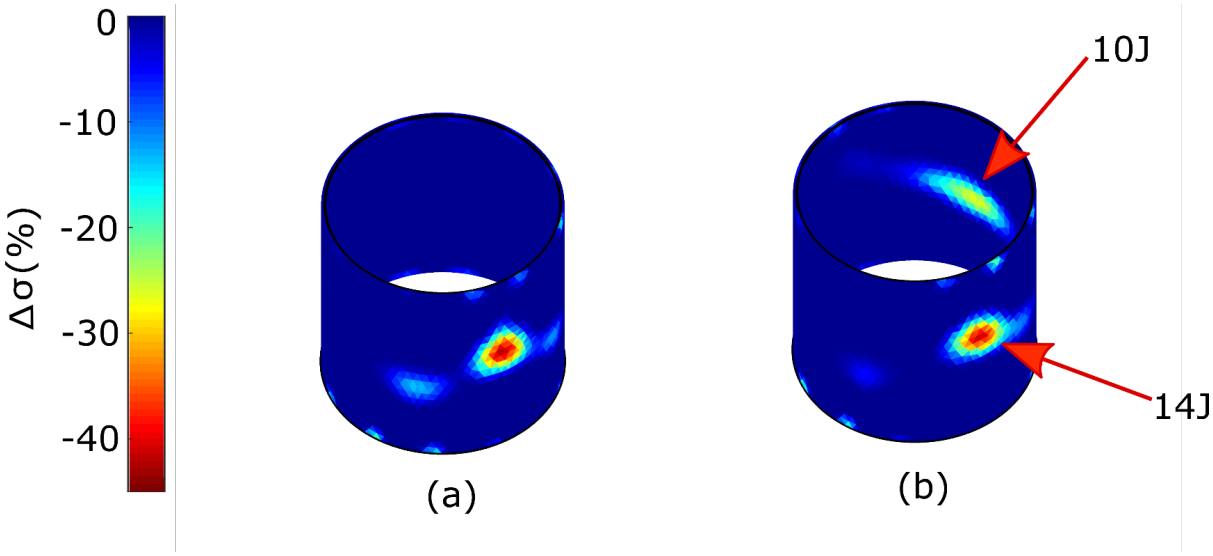

Figure 5.16: EIT reconstruction of the post-impacted tube (a) 14 J impact (b) 14 J and 10 J impact.

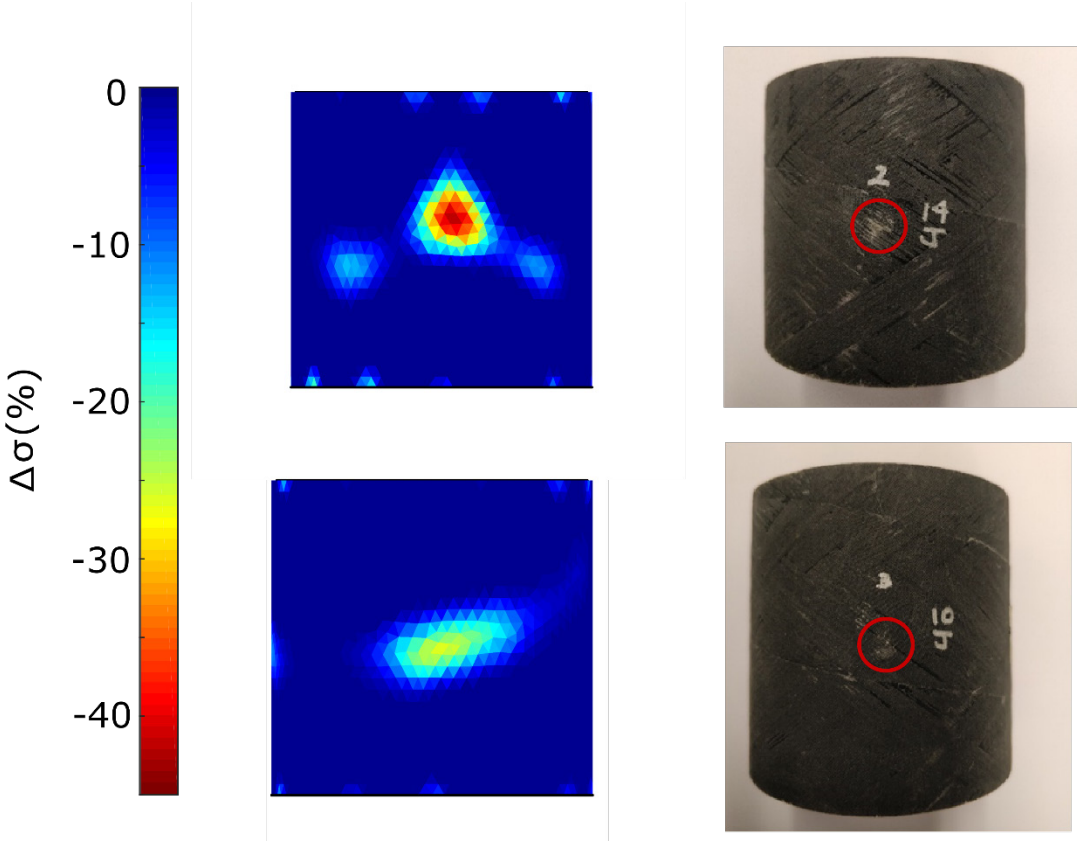

Figure 5.17: Figure showing the comparison of the conductivity reconstructions and the actual impacted location.

6. SUMMARY, CONCLUSIONS, AND FUTURE WORK

6.1 Summary

This research presents a critical advancement to the state of the art for conductivity based SHM by exploring the feasibility of employing EIT for damage detection in self-sensing filament-wound glass/fiber epoxy tubes. The work was motivated by the growing importance of composite tubes in potentially high-risk applications, the limitations of prevailing SHM modalities for composite tubes, the potential of self-sensing materials for composite tube SHM, and the overwhelming lack of work on non-planar EIT.

After initially developing a mathematical framework to conduct EIT, a tube of length-to-diameter ratio 2:1 was cut. Holes of diameter 4.76 mm, 7.94 mm and 9.53 mm were drilled at three different locations. It was observed that the holes near the center went undetected whereas the holes near the edges were clearly detectable. Multiple damage locations were also detectable; however, the results suggested that EIT lost sensitivity to damage near the center for long tubes. To further explore the effect of specimen length on EIT sensitivity, tubes of length-to-diameter ratio of 1:1 and 3:2 were studied. Through-holes of diameter 4.76 mm, 7.94 mm, and holes of 9.53 mm were drilled at the center of both the specimens. All holes were clearly detectable in the specimen of length to dimeter ratio of 1:1 whereas the 4.76 mm hole went undetected for the 3:2 specimen. This confirmed the supposition that EIT loses sensitivity to damage near the center with increasing length of the specimen.

Finally, BVID was induced by low velocity impacts on a tube with length-to-diameter ratio of 1:1. The tube was first impacted with 14 J and then again with 10 J at a different location. EIT was able to successfully detect damages from both the impacts with conductivity change magnitudes increasing with impact energy.

6.2 Conclusion

In conclusion, this study shows EIT can be used for damage detection in non-planar multiply connected domains. This study is of enormous importance in establishing EIT as a versatile SHM

and NDE modality. With the abundance of literature in using EIT for damage detection in planar structures, this study advances the state of the art in conductivity based SHM using EIT to more complex shapes representative of real world geometries.

6.3 Future Work

The current work extended the use of EIT to a composite tube without altering the underlying mathematical framework of EIT. The author believes that performance could be improved by altering the mathematical framework to suit the geometry at hand. For example, based on the constrained sine wave formulation presented by Tallman and Wang [66], cylindrical harmonics could be a potential strategy for cylindrical specimens. Further, the inverse problem herein presented is very sensitive to the conductivity bounds. It is postulated that the non-planar geometry exacerbates the ill-posedness of the EIT inverse problem which precipitates this sensitivity, but this is uncertain at this point. Hence, optimization strategies for EIT, especially in non-planar geometries would be an interesting study.

Further, an elemental based mapping could be developed for anisotropic conductivity. The current work assumes isotropic conductivity. The assumption holds reasonably well in this study as we see a good correlation between the forward model and the experimental voltages. However, if carbon fibers were used instead of glass fibers, the conductivity tensor woulds be much more complex, depending on the orientation and volume fraction of the continuous fiber. To that end, finding homogenized conductivity values and mapping these conductivity values to the EIT mesh would be an appropriate method to tackle anisotropic conductivity. Studies similar to [55], [56] and [58] could be extended to filament wound composites to tackle anisotropic conductivity.

APPENDIX A. DETAILED FORWARD PROBLEM

This appendix looks at the detailed formulation of the forward problem. Indicial notations are used in the equations. However, while forming the matrices for the finite element formulation, the indicial notation has been dropped due to the large number of subscripts and super scripts. These derivations are adapted from [67].

A.1 Steady State Diffusion Weak Form and Discretization

The domain equation for steady state diffusion in given by

$$\frac{-\partial j_i}{\partial x_i} = \frac{\partial}{\partial x_i}\sigma_{ij}\frac{\partial u}{\partial x_i} = f \tag{A.1}$$

Here, j_i is the current density vector, σ_{ij} is the conductivity tensor, u is the domain potential, and f is an internal current source. Conservation of charge is enforced to maintain current entering the electrodes is equal to the current leaving the electrodes. It is assumed that no current flows through the boundaries where no electrodes are attached. These condition are enforced as follows.

$$\int_{E_l} \sigma_{ij}\frac{\partial u}{\partial x_i} n_j \mathrm{d}S_l = I_l \tag{A.2}$$

$$\sigma_{ij}\frac{\partial u}{\partial x_i} n_j = 0 \text{ off } \cup_{l=1}^{L} E_l \tag{A.3}$$

$$\sum_{l=1}^{L} I_l = 0 \tag{A.4}$$

Here, n_j is the outward pointing normal and L is the total number of electrodes. Now the weak form is formulated by multiplying equation (A.1) by a weighting function ψ that satisfies the Dirichlet boundary conditions and integrating over the domain.

$$\int_{\Omega} \psi \frac{\partial}{\partial x_j}\sigma_{ij}\frac{\partial u}{\partial x_i}\mathrm{d}\Omega = \int_{\Omega} \psi f d\Omega \tag{A.5}$$

Since internal current sources are absent, the forcing vector, $f = 0$. Using Green's identity and the distribution property of derivatives, (A.5) becomes

$$\int_{\Omega} \frac{\partial}{\partial x_j} \psi \sigma_{ij} \frac{\partial u}{\partial x_i} \mathrm{d}\Omega - \int_{\Omega} \frac{\partial \psi}{\partial x_i} \sigma_{ij} \frac{\partial u}{\partial x_j} \mathrm{d}\Omega = 0 \tag{A.6}$$

Applying the Divergence's theorem to equation (A.6) we have,

$$\int_{\Omega} \frac{\partial \psi}{\partial x_i} \sigma_{ij} \frac{\partial u}{\partial x_i} \mathrm{d}\Omega = \int_{\partial\Omega} \psi \sigma_{ij} \frac{\partial u}{\partial x_i} n_j \mathrm{d}S = \int_{\Gamma} \sigma_{ij} \frac{\partial u}{\partial x_j} n_j \psi \mathrm{d}S \tag{A.7}$$

where $\Gamma = \cup_{l=1}^{L} E_l$ is the union of electrodes. Substituting, equation (4.2), the CEM interface equation, into equation (A.7) we have the following equation.

$$\int_{\Omega} \frac{\partial \psi}{\partial x_i} \sigma_{ij} \frac{\partial u}{\partial x_i} \mathrm{d}\Omega = \sum_{l=1}^{L} \int_{E_l} \frac{1}{z_l} (V_l - u)\ \psi \mathrm{d}S_l \tag{A.8}$$

Now, equation (A.8) is discretized by dividing the domain into subsets described by Ω_e. The assembly of subsets over the domain is represented by equation (A.9)

$$\sum_e \int_{\Omega_e} \frac{\partial \psi_e}{\partial x_i} \sigma_{ij} \frac{\partial u_e}{\partial x_j} \mathrm{d}\Omega_e = \sum_e \sum_{l=1}^{L} \int_{\partial\Omega_e} \frac{1}{z_l} (V_l - u_e)\ \psi_e \mathrm{d}S_e \tag{A.9}$$

Now, u_e and ψ_e are expressed via interpolating functions. These formulations are given in equations (A.10) and (A.11)

$$u_e = \sum_{A=1}^{N} \omega^A d_e^A \tag{A.10}$$

$$\psi_e = \sum_{A=1}^{N} \omega^A c_e^A \tag{A.11}$$

Here, d_e^A is the nodal solution of the Ath node for the eth element, and c_e^A is the variation of the Ath node for the eth element. The interpolation of the nodal solutions are given by equation (A.10).

A.2 Forming the Finite Element Matrices

Equations (A.10) and (A.11) are substituted into the left hand side of equation (A.9) to give the following.

$$\int_{\Omega_e} \frac{\partial \psi_e}{\partial x_i} \sigma_{ij} \frac{\partial u_e}{\partial x_j} \mathrm{d}\Omega_e = \sum_{A=1}^{N} \sum_{B=1}^{N} c_e^A \int_{\Omega_e} \frac{\partial \omega^A}{\partial x_i} \sigma_{ij} \frac{\partial \omega^B}{\partial x_j} \mathrm{d}\Omega_e \, d_e^B \tag{A.12}$$

Since c_e^A and d_e^A are constants they are pulled out of the domain. Also, the interpolation functions are defined on an isoparametric domain given by

$$x_i = \sum_{A=1}^{N} \omega^A(\zeta) x_i^A \tag{A.13}$$

Now the chain rule of differentiation can be used to define the gradients of the interpolation functions.

$$\frac{\partial \omega^A}{\partial x_i} = \frac{\partial \omega^A}{\partial \zeta_j} \frac{\partial \zeta_j}{\partial x_i} \tag{A.14}$$

$\partial \zeta_j / \partial x_i$ is the inverse of $\partial x_j / \partial \zeta_i$ and is formed by differentiating equation (A.13). Equation (A.12) is now rewritten as follows.

$$\int_{\Omega_e} \frac{\partial \psi_e}{\partial x_i} \sigma_{ij} \frac{\partial u_e}{\partial x_j} \mathrm{d}\Omega_e = \sum_{A=1}^{N} \sum_{B=1}^{N} c_e^A \int_{\Omega_e} \frac{\partial \omega^A}{\partial \zeta_k} \frac{\partial \zeta_k}{\partial x_i} \sigma_{ij} \frac{\partial \omega^B}{\partial \zeta_l} \frac{\partial \zeta_l}{\partial x_j} \mathrm{d}\Omega_e d_e^B \tag{A.15}$$

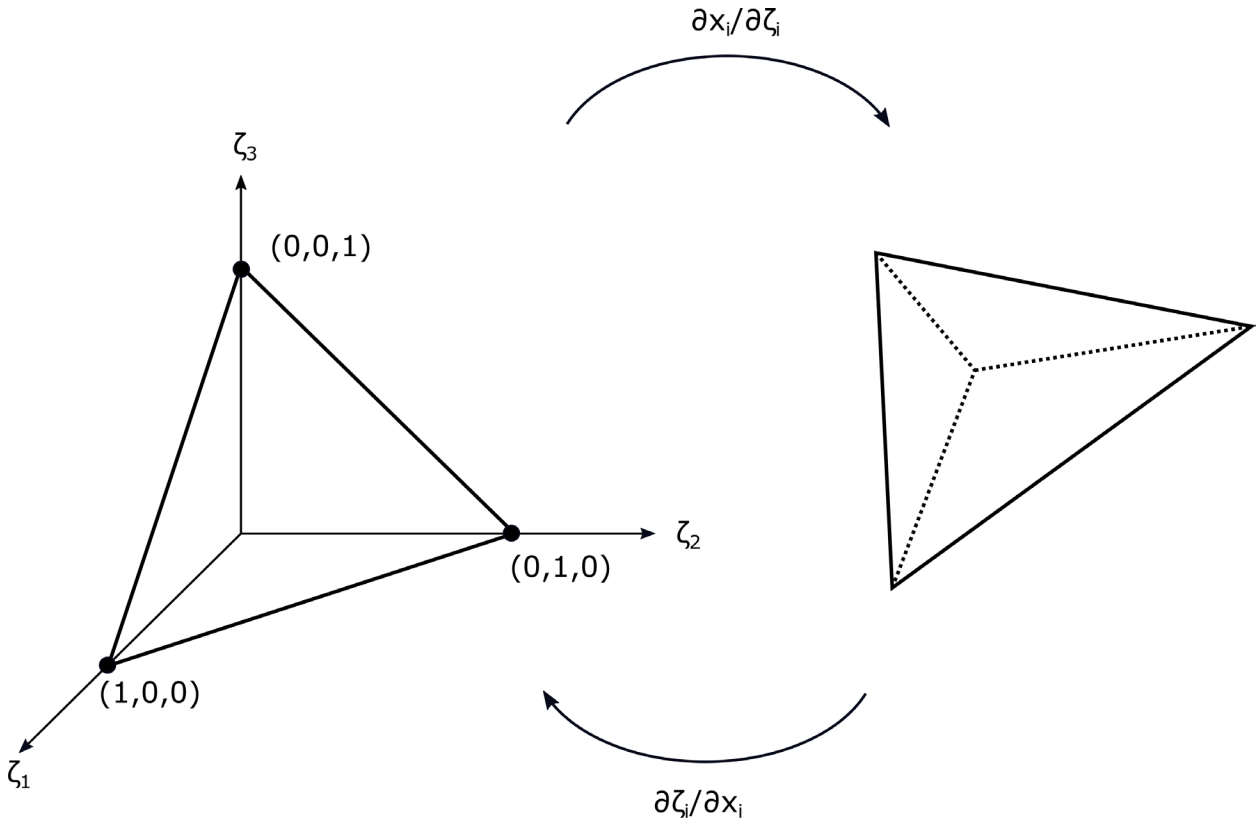

Figure A.1: A tetrahedral element shown to the right is mapped to the isoparametric domain shown to the left.

Since isoparametric domains are used, the integrals can be exactly calculated using numerical quadrature with appropriately selected Lagrange functions. Linear tetrahedral elements are used in this research given by, $\omega^1 = \zeta_1$, $\omega^2 = \zeta_2$, $\omega^3 = \zeta_3$ and $\omega^4 = 1 - \zeta_1 - \zeta_2 - \zeta_3$. Expressing the integrals in the isoparametric domain requires the multiplication by the volume of the tetrahedral element given by $\det|\partial x_m/\partial \zeta_n|$. Hence, equation (A.15) is represented as follows

$$\int_{\Omega_e} \frac{\partial \psi_e}{\partial x_i} \sigma_{ij} \frac{\partial u_e}{\partial x_j} \mathrm{d}\Omega_e = \sum_{A=1}^{N} \sum_{B=1}^{N} c_e^A \int_{\Omega_{e_\zeta}} \frac{\partial \omega^A}{\partial \zeta_k} \frac{\partial \zeta_k}{\partial x_i} \sigma_{ij} \frac{\partial \omega^B}{\partial \zeta_l} \frac{\partial \zeta_l}{\partial x_j} \det\left|\frac{\partial x_m}{\partial \zeta_n}\right| \mathrm{d}\Omega_{e_\zeta} d_e^B \quad \text{(A.16)}$$

Here, Ω_{e_ζ} is the integration of the eth element in isoparametric domain. Since, linear interpolation elements are used, the gradients are constant, which are pre-calculated. However, for extending this method to higher order polynomial interpolation functions the numerical quadrate is used and

is given in equation (A.17). The numerical quadrature will be also needed, if readers want to replicate the current work with hexahedral elements.

$$\int_{\Omega_{e_\zeta}} p(\zeta_i)\,\mathrm{d}\Omega_{e_\zeta} = \sum_m^M a_m p(\zeta_m) \tag{A.17}$$

Here the summation runs over the number of quadrate points and a_m is the mth weight. Looking at equation (A.16), we now have all the integrals calculated and it can be evaluated to form the elemental diffusion stiffness matrix.

$$\int_{\Omega_e} \frac{\partial \psi_e}{\partial x_i}\sigma_{ij}\frac{\partial u_e}{\partial x_j}\,\mathrm{d}\Omega_e = \sum_{A=1}^{N}\sum_{B=1}^{N} c_e^A\, k_e^{AB}\, d_e^B = [c_e^1\ c_e^2\ \cdots\ c_e^N]k_e\begin{bmatrix} d_e^1 \\ d_e^2 \\ \vdots \\ d_e^N \end{bmatrix} \tag{A.18}$$

Here k_e^{AB} is the local diffusion matrix of the eth element and can be assembled into the global diffusion matrix, A_M. The local stiffness diffusion matrix for the eth element is shown in equation (A.19)

$$\begin{aligned} k_e = \frac{1}{6}&\begin{bmatrix} 1 & 0 & 0 \\ 0 & 1 & 0 \\ 0 & 0 & 1 \\ -1 & -1 & -1 \end{bmatrix}\begin{bmatrix} x_1^e - x_4^e & x_2^e - x_4^e & x_3^e - x_4^e \\ y_1^e - y_4^e & y_2^e - y_4^e & y_3^e - y_4^e \\ z_1^e - z_4^e & z_2^e - z_4^e & z_3^e - z_4^e \end{bmatrix}^{-1} \cdots \\ \cdots&\begin{bmatrix} \sigma_{11} & \sigma_{12} & \sigma_{13} \\ \sigma_{21} & \sigma_{22} & \sigma_{23} \\ \sigma_{31} & \sigma_{32} & \sigma_{33} \end{bmatrix}\left[\begin{bmatrix} x_1^e - x_4^e & x_2^e - x_4^e & x_3^e - x_4^e \\ y_1^e - y_4^e & y_2^e - y_4^e & y_3^e - y_4^e \\ z_1^e - z_4^e & z_2^e - z_4^e & z_3^e - z_4^e \end{bmatrix}^{-T}\right] \cdots \\ \cdots&\begin{bmatrix} 1 & 0 & 0 \\ 0 & 1 & 0 \\ 0 & 0 & 1 \\ -1 & -1 & -1 \end{bmatrix}^T \det\left|\begin{bmatrix} x_1^e - x_4^e & x_2^e - x_4^e & x_3^e - x_4^e \\ y_1^e - y_4^e & y_2^e - y_4^e & y_3^e - y_4^e \\ z_1^e - z_4^e & z_2^e - z_4^e & z_3^e - z_4^e \end{bmatrix}\right| \end{aligned} \tag{A.19}$$

Also, the volume of the tetrahedral element, $\det|\partial x_m/\partial \zeta_n|$, is given by

$$V^e = \frac{1}{6}\det\left|\begin{bmatrix} x_1^e - x_4^e & x_2^e - x_4^e & x_3^e - x_4^e \\ y_1^e - y_4^e & y_2^e - y_4^e & y_3^e - y_4^e \\ z_1^e - z_4^e & z_2^e - z_4^e & z_3^e - z_4^e \end{bmatrix}\right| \tag{A.20}$$

Now we move on to the formation of A_Z, A_W and A_D. These matrices are formed by returning to equation (A.9) and evaluating the right hand side of the equation.

$$\sum_e \int_{\partial\Omega_e} \frac{1}{z_l}(V_l - u_e)\psi_e \,\mathrm{d}S_e = \sum_e \left(-\int_{\partial\Omega_e} \frac{1}{z_l} u_e \psi_e \,\mathrm{d}S_e + \int_{\partial\Omega_e} \frac{1}{z_l} V_l \psi_e \,\mathrm{d}S_e\right) \tag{A.21}$$

It is important to point out that while forming A_Z and A_W we used interpolation functions that are one degree lower than the degree used in the domain discretization. Since we used $\omega^1 = \zeta_1$, $\omega^2 = \zeta_2$, $\omega^3 = \zeta_3$ and $\omega^4 = 1 - \zeta_1 - \zeta_2 - \zeta_3$ for the domain we use $\omega^1 = \zeta_1$, $\omega^2 = \zeta_2$, $\omega^3 = 1 - \zeta_1 - \zeta_2$ for the formation of A_Z and A_W. Further, we move the right hand side of equation (A.21) to the left hand side of equation (A.9) and substitute the expressions from (A.10) and (A.11). The process follows the similar variational procedure as outlined for the formation of A_M and only the final results are shown here.

To form A_Z, we use the first integral on the right hand side of equation (A.21) and consider the eth element of the lth electrode.

$$\int_{\partial\Omega_e} \frac{1}{z_l} u_e \psi_e \,\mathrm{d}S_e = \sum_{A=1}^{N}\sum_{B=1}^{N} c_e^A \int_{\Omega_e} \frac{1}{z_l}\omega^A\omega^B \,\mathrm{d}S_e d_e^B = [c_e^1 \;\; c_e^2 \;\cdots\; c_e^N] A_Z^{el} \begin{bmatrix} d_e^1 \\ d_e^2 \\ \vdots \\ d_e^N \end{bmatrix} \tag{A.22}$$

The integral in equation (A.22) is evaluated to find the A_Z matrix for the eth element on the lth electrode.

$$A_Z^{el} = \int_0^1 \int_0^{1-\zeta_1} \frac{2A^e}{z_l} \begin{bmatrix} \zeta_1^2 & \zeta_1\zeta_2 & \zeta_1(1-\zeta_1-\zeta_2) \\ \zeta_1\zeta_2 & \zeta_2^2 & \zeta_2(1-\zeta_1-\zeta_2) \\ \zeta_1(1-\zeta_1-\zeta_2) & \zeta_2(1-\zeta_1-\zeta_2) & (1-\zeta_1-\zeta_2)^2 \end{bmatrix} \mathrm{d}\zeta_2 \mathrm{d}\zeta_1$$

$$= \frac{A^e}{12_{z_l}} \begin{bmatrix} 2 & 1 & 1 \\ 1 & 2 & 1 \\ 1 & 1 & 2 \end{bmatrix} \tag{A.23}$$

Here, A^e is the area of the element. Here, we the integration over the domain leads to a multiplication by an area term, since the interpolating functions are a degree lower than the one used for domain discretization. After A_Z^{el} is formed for every other element in the electrode, the matrices are assembled into the global A_Z matrix.

A_W links the domain voltage to the electrode voltages. To form A_W, the second integral on the right hand side of equation (A.21) is evaluated. Now, consider the eth element of the lth electrode.

$$-\int_{\Omega_e} \frac{1}{z_l} u_e \, V_e \mathrm{d}S_e = -\sum_{A=1}^{N} c_e^A \int_{\Omega_e} \frac{1}{z_l} \omega^A \mathrm{d}S_e V_l = [c_e^1 \;\; c_e^2 \;\cdots\; c_e^N] A_W^{el} V_l \tag{A.24}$$

The electrode voltages, V_l are pulled out of the integral since they are assumed to be constant. The explicit form of A_W^{el} after evaluating the integrals is given by

$$A_W^{el} = \int_0^1 \int_0^{1-\zeta_1} \frac{2A^e}{z_l} \begin{bmatrix} \zeta_1 \\ \zeta_2 \\ 1-\zeta_1-\zeta_2 \end{bmatrix} \mathrm{d}\zeta_2 \mathrm{d}\zeta_1$$

$$= \frac{A^e}{3z_l} \begin{bmatrix} 1 \\ 1 \\ 1 \end{bmatrix} \tag{A.25}$$

As shown in equation (A.25) A_W^{el} has 3 rows and 1 column, where the number of correspond to the nodes in an element of the electrode l. To form the global A_W matrix, A_W^{el} has to be evaluated for all the elements in a an electrode and then this has to be repeated for every electrode. Hence the size of the global A_W has the total number of nodes in the simulation as the number of rows and the total number of electrodes as the number of columns.

Further, A_D relates the electrode voltages to the electrode current. The current through the lth electrode is given by

$$I_l = \int_{E_l} \frac{1}{z_l}(V_l - u)\ \mathrm{d}S_l = \frac{1}{z_l}E_l V_l - \int_{E_l} \frac{1}{z_l} u\, \mathrm{d}S_l \tag{A.26}$$

By assuming a constant contact impedance and electrode voltage, the first term in the right hand side of equation (A.26) relates the electrode current to the electrode voltage by E_l/z_l. This accounts for the equation of A_D.

APPENDIX B. DETAILED INVERSE PROBLEM

B.1 Forming the Sensitivity Matrix Entries

The formation of the sensitivity matrix is similar to the formation of the diffusion stiffness matrix discussed in appendix A. However, the explicit forms of the matrices are discussed here. We recall equation (4.18) which was for the case of isotropic conductivity. The general case with anisotropic conductivity is given by equation (B.1)

$$J_{MN_e} = -\int_{\Omega_e} \frac{\partial u^M}{\partial x_i} \sigma_{ij} \frac{\partial \bar{u}^N}{\partial x_j} \mathrm{d}\Omega_e \tag{B.1}$$

We now substitute the equation (A.10) in equation (B.1). in doing so we get equation (B.2). Note that the number of nodes per element is given by Nn here to avoid using the same indices for J_{MN_e}

$$J_{MN_e} = -\sum_{A=1}^{Nn} \sum_{B=1}^{Nn} d_e^{AM} \int_{\Omega_e} \frac{\partial \omega^A}{\partial x_i} \sigma_{ij} \frac{\partial \omega^B}{\partial x_j} \mathrm{d}\Omega_e \bar{d}_e^{BN} \tag{B.2}$$

d_e^{AM} refers to the Ath nodal solution of the eth element due to the Mth current injection and $\bar{d}_e^{BN}$ refers to the Bth nodal solution of the eth element due to a unit current injection at the Nth electrode pair. Now the gradients are calculates similar to the procedure followed in forming the stiffness matrix for the forward problem. On carrying out the differentiation we get equation (B.3). Again the integration is carried out in the isoparametric domain and since the interpolating functions are linear polynomials their gradients are constant.

$$-\int_{\Omega_e} \frac{\partial u^M}{\partial x_i} \sigma_{ij} \frac{\partial \bar{u}^N}{\partial x_j} \mathrm{d}\Omega_e = -\sum_{A=1}^{Nn} \sum_{B=1}^{Nn} d_e^{AM} \int_{\Omega_e} \frac{\partial \omega^A}{\partial \zeta_k} \frac{\partial \zeta_k}{\partial x_i} \sigma_{ij} \frac{\partial \omega^B}{\partial \zeta_l} \frac{\partial \zeta_l}{\partial x_j} \det\left|\frac{\partial x_m}{\partial \zeta_n}\right| \mathrm{d}\Omega_e \bar{d}_e^{BN} \tag{B.3}$$

The summation is now expressed in the terms of matrices given as follows.

$$-\int_{\Omega_e}\frac{\partial u^Q}{\partial x_i}\sigma_{ij}\frac{\partial \overline{u}^R}{\partial x_j}\mathrm{d}\Omega_e = -\sum_{A=1}^{N}\sum_{B=1}^{N} d_e^{AQ}\, j_e^{AB}\, d_e^{BR} = \left[d_e^{1Q}\ d_e^{2Q}\ \ldots\ d_e^{NQ}\right]\mathrm{j_e}\begin{bmatrix}\overline{d}_e^{1R}\\ \overline{d}_e^{2R}\\ \vdots\\ \overline{d}_e^{NR}\end{bmatrix} \quad \text{(B.4)}$$

As mentioned earlier the gradients are pre-calculated and hence the explicit form of an entry in the sensitivity matrix is given by equation (B.5). While it may be obvious to readers, it is worth mentioning that the form of j_e gives a scalar and not a matrix, as previously obtained for the stiffness matrix in the forward problem.

$$\begin{aligned}\mathrm{j_e} = -\frac{1}{6}&\begin{bmatrix}1 & 0 & 0\\ 0 & 1 & 0\\ 0 & 0 & 1\\ -1 & -1 & -1\end{bmatrix}\begin{bmatrix}x_1^e & -x_4^e & x_2^e & -x_4^e & x_3^e & -x_4^e\\ y_1^e & -y_4^e & y_2^e & -y_4^e & y_3^e & -y_4^e\\ z_1^e & -z_4^e & z_2^e & -z_4^e & z_3^e & -z_4^e\end{bmatrix}^{-1}\ \ldots\\ \ldots&\begin{bmatrix}\sigma_{11} & \sigma_{12} & \sigma_{13}\\ \sigma_{21} & \sigma_{22} & \sigma_{23}\\ \sigma_{31} & \sigma_{32} & \sigma_{33}\end{bmatrix}\left[\begin{bmatrix}x_1^e & -x_4^e & x_2^e & -x_4^e & x_3^e & -x_4^e\\ y_1^e & -y_4^e & y_2^e & -y_4^e & y_3^e & -y_4^e\\ z_1^e & -z_4^e & z_2^e & -z_4^e & z_3^e & -z_4^e\end{bmatrix}^{-T}\right.\ \ldots\\ \ldots&\left.\begin{bmatrix}1 & 0 & 0\\ 0 & 1 & 0\\ 0 & 0 & 1\\ -1 & -1 & -1\end{bmatrix}^{T}\right]\det\left|\begin{bmatrix}x_1^e & -x_4^e & x_2^e & -x_4^e & x_3^e & -x_4^e\\ y_1^e & -y_4^e & y_2^e & -y_4^e & y_3^e & -y_4^e\\ z_1^e & -z_4^e & z_2^e & -z_4^e & z_3^e & -z_4^e\end{bmatrix}\right|\end{aligned} \quad \text{(B.5)}$$

B.1 Gauss- Newton method

Mathematically, the Gauss Newton method iteratively updates a conductivity estimate to minimize the difference between the experimental voltage measurements and the numerically predicted voltage measurements. A major difference in the Gauss Newton method is that the forward operator is run iteratively which gets information from the updated conductivity distribution. Again, here the minimization is performed in the least-squares sense and is shown in equation (B.6)

$$\boldsymbol{\sigma}^* = \arg\min\left(\|\boldsymbol{V}_m - F(\boldsymbol{\sigma})\|^2\right) \quad \text{(B.6)}$$

Again, here $\boldsymbol{V}_m$ is the vector of experimentally predicted voltages and, $\boldsymbol{F}(\boldsymbol{\sigma})$ is a vector of voltages predicted by the forward model. Considering the Taylor series expansion as explained earlier for the forward problem we rewrite equation (B.6) as shown in equation (B.7)

$$\boldsymbol{\sigma}^* = \arg\min \left\| \boldsymbol{V}_m - \left(\boldsymbol{F}(\boldsymbol{\sigma_0}) + \frac{\partial \boldsymbol{F}(\sigma_0)}{\partial \boldsymbol{\sigma}} (\boldsymbol{\sigma} - \boldsymbol{\sigma}_0) \right) \right\|^2 \tag{B.7}$$

Following the same procedure as described in Chapter 4, section 4.3 we rewrite equation (B.7) as shown in equation (B.8)

$$\boldsymbol{\sigma}^* = \arg\min \|\boldsymbol{V}_m - \boldsymbol{J}\Delta\boldsymbol{\sigma}\|^2 \tag{B.8}$$

In the above equation we have replaced $\boldsymbol{\sigma} - \boldsymbol{\sigma}_0$ by $\boldsymbol{\Delta\sigma}$ and $\boldsymbol{V_m} - \boldsymbol{F}(\boldsymbol{\sigma}) = \boldsymbol{V_e}$. Again the solution retrieval process requires a regularization and the explicit solution is given by equation (B.9)

$$\Delta\boldsymbol{\sigma} = (\boldsymbol{J^T J} + \boldsymbol{\alpha^2 L^T L}\ )^{-1} \boldsymbol{J^T V_e} \tag{B.9}$$

The conductivity estimate is then updated as shown in equation (B.10) until the error between the model predictions and the experimental measurements are sufficiently minimized.

$$\boldsymbol{\sigma}^*_{\boldsymbol{n+1}} = \boldsymbol{\sigma}^*_{\boldsymbol{n}} + \Delta\boldsymbol{\sigma} \tag{B.10}$$

Although the Gauss-Newton method aims to reconstruct the absolute conductivity of the damaged state, reconstructions showing absolute conductivity is not generally reported. This is because the absolute conductivity images contain erroneous data arising from discrepancies between the finite element model and the actual specimen. Hence the conductivity is reconstructed at two distinct times (similar to the method mentioned in section 4.3) and the difference of images is reported. This procedure allows for the common errors arising from electrode placements to be cancelled out.

REFERENCES

[1] V. V. Vasiliev, A. A. Krikanov, and A. F. Razin, "New generation of filament-wound composite pressure vessels for commercial applications," *Compos. Struct.*, vol. 62, no. 3–4, pp. 449–459, 2003.

[2] F. Taheri, "Advanced fiber-reinforced polymer (FRP) composites for the manufacture and rehabilitation of pipes and tanks in the oil and gas industry," in *Advanced Fibre-Reinforced Polymer (FRP) Composites for Structural Applications*, Elsevier, 2013, pp. 662–704.

[3] H. Bakaiyan, H. Hosseini, and E. Ameri, "Analysis of multi-layered filament-wound composite pipes under combined internal pressure and thermomechanical loading with thermal variations," *Compos. Struct.*, vol. 88, no. 4, pp. 532–541, 2009.

[4] L. Gemi, "Investigation of the effect of stacking sequence on low velocity impact response and damage formation in hybrid composite pipes under internal pressure. A comparative study," *Compos. Part B Eng.*, vol. 153, pp. 217–232, 2018.

[5] K. L. Alderson and K. E. Evans, "Failure mechanisms during the transverse loading of filament-wound pipes under static and low velocity impact conditions," *Composites*, vol. 23, no. 3, pp. 167–173, 1992.

[6] J. Curtis, M. J. Hinton, S. Li, S. R. Reid, and P. D. Soden, "Damage, deformation and residual burst strength of filament-wound composite tubes subjected to impact or quasi-static indentation," *Compos. Part B Eng.*, vol. 31, no. 5, pp. 419–433, 2000.

[7] A. Vashisth, C. E. Bakis, C. R. Ruggeri, T. C. Henry, and G. D. Roberts, "Ballistic impact response of carbon/epoxy tubes with variable nanosilica content," *J. Compos. Mater.*, vol. 52, no. 12, pp. 1589–1604, 2018.

[8] M. Tarfaoui, P. B. Gning, and L. Hamitouche, "Dynamic response and damage modeling of glass/epoxy tubular structures: Numerical investigation," *Compos. Part Appl. Sci. Manuf.*, vol. 39, no. 1, pp. 1–12, 2008.

[9] M. Tarfaoui, P.-B. Gning, P. Davies, and F. Collombet, "Scale and size effects on dynamic response and damage of glass/epoxy tubular structures," *J. Compos. Mater.*, vol. 41, no. 5, pp. 547–558, 2007.

[10] S. Benli, M. Özen, O. Sayman, and M. E. Deniz, "Determination of mechanical properties and failure pressure in composite cylinders," *Mater. Test.*, vol. 54, no. 1, pp. 41–44, 2012.

[11] E. P. Carden and P. Fanning, "Vibration based condition monitoring: a review," *Struct. Health Monit.*, vol. 3, no. 4, pp. 355–377, 2004.

[12] "Montalvao, D., Maia, N. M. M., and Ribeiro, A. M. R., 'A review of vibration-based ˜ structural health monitoring with special emphasis on composite materials,' Shock and Vibration Digest, Vol. 38, No. 4, 2006, pp. 295–326.

[13] B.-H. Choi and I.-B. Kwon, "Strain pattern detection of composite cylinders using optical fibers after low velocity impacts," *Compos. Sci. Technol.*, vol. 154, pp. 64–75, 2018.

[14] G. Luyckx, E. Voet, N. Lammens, and J. Degrieck, "Strain measurements of composite laminates with embedded fibre Bragg gratings: Criticism and opportunities for research," *Sensors*, vol. 11, no. 1, pp. 384–408, 2011.

[15] H. Tsuda and J.-R. Lee, "Strain and damage monitoring of CFRP in impact loading using a fiber Bragg grating sensor system," *Compos. Sci. Technol.*, vol. 67, no. 7–8, pp. 1353–1361, 2007.

[16] H. Hernández-Moreno, F. Collombet, B. Douchin, D. Choqueuse, P. Davies, and J. G. Velázquez, "Entire life time monitoring of filament wound composite cylinders using Bragg grating sensors: I. Adapted tooling and instrumented specimen," *Appl. Compos. Mater.*, vol. 16, no. 3, pp. 173–182, 2009.

[17] S. Beard and F.-K. Chang, "Active damage detection in filament wound composite tubes using built-in sensors and actuators," *J. Intell. Mater. Syst. Struct.*, vol. 8, no. 10, pp. 891–897, 1997.

[18] A. Raghavan, "Guided-wave structural health monitoring," 2007.

[19] G. Mook, R. Lange, and O. Koeser, "Non-destructive characterisation of carbon-fibre-reinforced plastics by means of eddy-currents," *Compos. Sci. Technol.*, vol. 61, no. 6, pp. 865–873, 2001.

[20] W. Yin, P. J. Withers, U. Sharma, and A. J. Peyton, "Noncontact characterization of carbon-fiber-reinforced plastics using multifrequency eddy current sensors," *IEEE Trans. Instrum. Meas.*, vol. 58, no. 3, pp. 738–743, 2008.

[21] E. T. Thostenson, C. Li, and T.-W. Chou, "Nanocomposites in context," *Compos. Sci. Technol.*, vol. 65, no. 3–4, pp. 491–516, 2005.

[22] M. H. Al-Saleh and U. Sundararaj, "Review of the mechanical properties of carbon nanofiber/polymer composites," *Compos. Part Appl. Sci. Manuf.*, vol. 42, no. 12, pp. 2126–2142, 2011.

[23] A. K.-T. Lau and D. Hui, "The revolutionary creation of new advanced materials—carbon nanotube composites," *Compos. Part B Eng.*, vol. 33, no. 4, pp. 263–277, 2002.

[24] T. W. Ebbesen, H. J. Lezec, H. Hiura, J. W. Bennett, H. F. Ghaemi, and T. Thio, "Electrical conductivity of individual carbon nanotubes," *Nature*, vol. 382, no. 6586, p. 54, 1996.

[25] E. T. Thostenson, Z. Ren, and T.-W. Chou, "Advances in the science and technology of carbon nanotubes and their composites: a review," *Compos. Sci. Technol.*, vol. 61, no. 13, pp. 1899–1912, 2001.

[26] S. Tsantzalis *et al.*, "On the improvement of toughness of CFRPs with resin doped with CNF and PZT particles," *Compos. Part Appl. Sci. Manuf.*, vol. 38, no. 4, pp. 1159–1162, 2007.

[27] F. H. Gojny, M. H. G. Wichmann, U. Köpke, B. Fiedler, and K. Schulte, "Carbon nanotube-reinforced epoxy-composites: enhanced stiffness and fracture toughness at low nanotube content," *Compos. Sci. Technol.*, vol. 64, no. 15, pp. 2363–2371, 2004.

[28] A. Liu, K. W. Wang, and C. E. Bakis, "Effect of functionalization of single-wall carbon nanotubes (SWNTs) on the damping characteristics of SWNT-based epoxy composites via multiscale analysis," *Compos. Part Appl. Sci. Manuf.*, vol. 42, no. 11, pp. 1748–1755, 2011.

[29] Y. Zhu, C. E. Bakis, and J. H. Adair, "Effects of carbon nanofiller functionalization and distribution on interlaminar fracture toughness of multi-scale reinforced polymer composites," *Carbon*, vol. 50, no. 3, pp. 1316–1331, 2012.

[30] Jkw. Sandler, J. E. Kirk, I. A. Kinloch, M. S. P. Shaffer, and A. H. Windle, "Ultra-low electrical percolation threshold in carbon-nanotube-epoxy composites," *Polymer*, vol. 44, no. 19, pp. 5893–5899, 2003.

[31] N. Hu, Z. Masuda, G. Yamamoto, H. Fukunaga, T. Hashida, and J. Qiu, "Effect of fabrication process on electrical properties of polymer/multi-wall carbon nanotube nanocomposites," *Compos. Part Appl. Sci. Manuf.*, vol. 39, no. 5, pp. 893–903, 2008.

[32] J.-C. Huang, "Carbon black filled conducting polymers and polymer blends," *Adv. Polym. Technol. J. Polym. Process. Inst.*, vol. 21, no. 4, pp. 299–313, 2002.

[33] J. G. Simmons, "Generalized formula for the electric tunnel effect between similar electrodes separated by a thin insulating film," *J. Appl. Phys.*, vol. 34, no. 6, pp. 1793–1803, 1963.

[34] W. Bauhofer and J. Z. Kovacs, "A review and analysis of electrical percolation in carbon nanotube polymer composites," *Compos. Sci. Technol.*, vol. 69, no. 10, pp. 1486–1498, 2009.

[35] J. Z. Kovacs, B. S. Velagala, K. Schulte, and W. Bauhofer, "Two percolation thresholds in carbon nanotube epoxy composites," *Compos. Sci. Technol.*, vol. 67, no. 5, pp. 922–928, 2007.

[36] N. Hu, Y. Karube, C. Yan, Z. Masuda, and H. Fukunaga, "Tunneling effect in a polymer/carbon nanotube nanocomposite strain sensor," *Acta Mater.*, vol. 56, no. 13, pp. 2929–2936, 2008.

[37] E. T. Thostenson and T.-W. Chou, "Aligned multi-walled carbon nanotube-reinforced composites: processing and mechanical characterization," *J. Phys. Appl. Phys.*, vol. 35, no. 16, p. L77, 2002.

[38] S. Gungor and C. E. Bakis, "Anisotropic networking of carbon black in glass/epoxy composites using electric field," *J. Compos. Mater.*, vol. 49, no. 5, pp. 535–544, 2015.

[39] E. T. Thostenson and T.-W. Chou, "Carbon nanotube networks: sensing of distributed strain and damage for life prediction and self healing," *Adv. Mater.*, vol. 18, no. 21, pp. 2837–2841, 2006.

[40] L. Gao, E. T. Thostenson, Z. Zhang, and T.-W. Chou, "Coupled carbon nanotube network and acoustic emission monitoring for sensing of damage development in composites," *Carbon*, vol. 47, no. 5, pp. 1381–1388, 2009.

[41] L. Gao, T.-W. Chou, E. T. Thostenson, Z. Zhang, and M. Coulaud, "In situ sensing of impact damage in epoxy/glass fiber composites using percolating carbon nanotube networks," *Carbon*, vol. 49, no. 10, pp. 3382–3385, 2011.

[42] D. Zhang, L. Ye, D. Wang, Y. Tang, S. Mustapha, and Y. Chen, "Assessment of transverse impact damage in GF/EP laminates of conductive nanoparticles using electrical resistivity tomography," *Compos. Part Appl. Sci. Manuf.*, vol. 43, no. 9, pp. 1587–1598, 2012.

[43] C. Viets, S. Kaysser, and K. Schulte, "Damage mapping of GFRP via electrical resistance measurements using nanocomposite epoxy matrix systems," *Compos. Part B Eng.*, vol. 65, pp. 80–88, 2014.

[44] T. I. Oh *et al.*, "Sub-millimeter resolution electrical conductivity images of brain tissues using magnetic resonance-based electrical impedance tomography," *Appl. Phys. Lett.*, vol. 107, no. 2, p. 023701, 2015.

[45] U. Krause, K. Becker, G. Hahn, J. Dittmar, W. Ruschewski, and T. Paul, "Monitoring of regional lung ventilation using electrical impedance tomography after cardiac surgery in infants and children," *Pediatr. Cardiol.*, vol. 35, no. 6, pp. 990–997, 2014.

[46] S. Maisch *et al.*, "Heart-lung interactions measured by electrical impedance tomography," *Crit. Care Med.*, vol. 39, no. 9, pp. 2173–2176, 2011.

[47] T.-C. Hou, K. J. Loh, and J. P. Lynch, "Spatial conductivity mapping of carbon nanotube composite thin films by electrical impedance tomography for sensing applications," *Nanotechnology*, vol. 18, no. 31, p. 315501, 2007.

[48] T.-C. Hou and J. P. Lynch, "Electrical impedance tomographic methods for sensing strain fields and crack damage in cementitious structures," *J. Intell. Mater. Syst. Struct.*, vol. 20, no. 11, pp. 1363–1379, 2009.

[49] A. Seppänen, K. Karhunen, A. Lehikoinen, J. P. Kaipio, and P. J. M. Monteiro, "Electrical resistance tomography imaging of concrete," in *Concrete Repair, Rehabilitation and Retrofitting II: 2nd International Conference on Concrete Repair, Rehabilitation and Retrofitting*, 2009, pp. 571–577.

[50] T. N. Tallman, S. Gungor, K. W. Wang, and C. E. Bakis, "Damage detection via electrical impedance tomography in glass fiber/epoxy laminates with carbon black filler," *Struct. Health Monit.*, vol. 14, no. 1, pp. 100–109, 2015.

[51] T. N. Tallman, S. Gungor, K. W. Wang, and C. E. Bakis, "Damage detection and conductivity evolution in carbon nanofiber epoxy via electrical impedance tomography," *Smart Mater. Struct.*, vol. 23, no. 4, p. 045034, 2014.

[52] B. R. Loyola, V. La Saponara, K. J. Loh, T. M. Briggs, G. O'Bryan, and J. L. Skinner, "Spatial sensing using electrical impedance tomography," *IEEE Sens. J.*, vol. 13, no. 6, pp. 2357–2367, 2013.

[53] B. R. Loyola *et al.*, "Detection of spatially distributed damage in fiber-reinforced polymer composites," *Struct. Health Monit.*, vol. 12, no. 3, pp. 225–239, 2013.

[54] M. Hallaji, A. Seppänen, and M. Pour-Ghaz, "Electrical impedance tomography-based sensing skin for quantitative imaging of damage in concrete," *Smart Mater. Struct.*, vol. 23, no. 8, p. 085001, 2014.

[55] S. Nonn, M. Schagerl, Y. Zhao, S. Gschossmann, and C. Kralovec, "Application of electrical impedance tomography to an anisotropic carbon fiber-reinforced polymer composite laminate for damage localization," *Compos. Sci. Technol.*, vol. 160, pp. 231–236, 2018.

[56] G. J. Gallo and E. T. Thostenson, "Spatial damage detection in electrically anisotropic fiber-reinforced composites using carbon nanotube networks," *Compos. Struct.*, vol. 141, pp. 14–23, 2016.

[57] T. N. Tallman, S. Gungor, G. M. Koo, and C. E. Bakis, "On the inverse determination of displacements, strains, and stresses in a carbon nanofiber/polyurethane nanocomposite from conductivity data obtained via electrical impedance tomography," *J. Intell. Mater. Syst. Struct.*, vol. 28, no. 18, pp. 2617–2629, 2017.

[58] T. N. Tallman, F. Semperlotti, and K. W. Wang, "Enhanced delamination detection in multifunctional composites through nanofiller tailoring," *J. Intell. Mater. Syst. Struct.*, vol. 26, no. 18, pp. 2565–2576, 2015.

[59] H. Hassan, F. Semperlotti, K.-W. Wang, and T. N. Tallman, "Enhanced imaging of piezoresistive nanocomposites through the incorporation of nonlocal conductivity changes in electrical impedance tomography," *J. Intell. Mater. Syst. Struct.*, vol. 29, no. 9, pp. 1850–1861, 2018.

[60] J. Cagáň, J. Pelant, M. Kyncl, M. Kadlec, and L. Michalcová, "Damage detection in carbon fiber–reinforced polymer composite via electrical resistance tomography with Gaussian anisotropic regularization," *Struct. Health Monit.*, p. 1475921718820013, 2018.

[61] T. N. Tallman and J. A. Hernandez, "The effect of error and regularization norms on strain and damage identification via electrical impedance tomography in piezoresistive nanocomposites," *NDT E Int.*, vol. 91, pp. 156–163, 2017.

[62] D. C. Dobson and F. Santosa, "Resolution and stability analysis of an inverse problem in electrical impedance tomography: dependence on the input current patterns," *SIAM J. Appl. Math.*, vol. 54, no. 6, pp. 1542–1560, 1994.

[63] A. Allers and F. Santosa, "Stability and resolution analysis of a linearized problem in electrical impedance tomography," *Inverse Probl.*, vol. 7, no. 4, p. 515, 1991.

[64] M. Vauhkonen, D. Vadasz, P. A. Karjalainen, E. Somersalo, and J. P. Kaipio, "Tikhonov regularization and prior information in electrical impedance tomography," *IEEE Trans. Med. Imaging*, vol. 17, no. 2, pp. 285–293, 1998.

[65] D. S. Holder, *Electrical impedance tomography: methods, history and applications*. CRC Press, 2004.

[66] T. N. Tallman and K. W. Wang, "Damage and strain identification in multifunctional materials via electrical impedance tomography with constrained sine wave solutions," *Struct. Health Monit.*, vol. 15, no. 2, pp. 235–244, 2016.

[67] T. N. Tallman, "Conductivity-Based Nanocomposite Structural Health Monitoring via Electrical Impedance Tomography," 2015.